



Spiess, R., Langone, A., Caggianelli, A., Stuart, F. M. , Zucchi, M., Bianco, C., Brogi, A. and Liotta, D. (2021) Unveiling ductile deformation during fast exhumation of a granitic pluton in a transfer zone. *Journal of Structural Geology*, 147, 104326.

(doi: [10.1016/j.jsg.2021.104326](https://doi.org/10.1016/j.jsg.2021.104326))

This is the Author Accepted Manuscript.

There may be differences between this version and the published version. You are advised to consult the publisher's version if you wish to cite from it.

<https://eprints.gla.ac.uk/237095/>

Deposited on: 19 March 2021

Unveiling ductile deformation during fast exhumation of a granitic pluton in a transfer zone

Richard Spiess^{1,*}, Antonio Langone², Alfredo Caggianelli³, Finlay M. Stuart⁴,
Martina Zucchi³, Caterina Bianco³, Andrea Brogi^{3,5}, Domenico Liotta^{3,5}

¹ Geosciences Department, University of Padova, Italy

² CNR-IGG, Institute of Geosciences and Earth Resources, Pavia

³ Department of Earth and Geoenvironmental Sciences, University of Bari, Italy

⁴ Isotope Geosciences, Scottish Universities Environmental Research Centre, East Kilbride, UK

⁵ CNR-IGG, Institute of Geosciences and Earth Resources, Pisa, Italy

* Corresponding author: richard.spiess@unipd.it

Abstract

Exhumation and cooling of upper crustal plutons is generally assumed to develop in the brittle domain, thus determining an abrupt passage from crystallization to faulting. To challenge this general statement, we applied an integrated approach involving meso- and micro-structural studies, thermochronology, geochronology and rheological modeling to the Miocene syn-tectonic Porto Azzurro pluton on Elba (Tuscan archipelago – Italy). This pluton is emplaced in an extensional setting, and we have realized that its fast exhumation is accompanied by localized ductile shear zones, developing along dykes and veins, later affected by brittle deformation. This is unequivocally highlighted by field studies and EBSD-aided microstructural analysis. To constrain the emplacement and exhumation rate of the Porto Azzurro pluton we performed U-Pb zircon dating and (U+Th)/He apatite thermochronology, which resulted in a magma emplacement age of 6.4 ± 0.4 Ma and an exhumation rate of 3.4 to 3.9 mm/yr. Thermo-rheological modeling established that localized ductile deformation occurred at two different time steps: within felsic dykes when the pluton first entered into the brittle field at 380 kyr, and along quartz-rich hydrothermal veins at c. 550 kyr after pluton emplacement. Hence, the major conclusion of our data is that ductile deformation can affect a granitic intrusion even when it is entered into the brittle domain in a fast exhuming extensional regime.

Key Words: Granite emplacement, fast exhumation, extensional tectonics, shearing, geochronology – thermochronology, rheological modeling.

1. Introduction

If strain rate is high ($\geq 1 \cdot 10^{-14} \text{ s}^{-1}$, Ranalli, 1995; Rey et al., 2009), extensional tectonics can be accompanied by high heat flow and diffuse emplacement of magmatic plutons at different structural levels, from the ductile lower crust to the brittle upper crust. In this framework, the migration of fluids is favored by the kinematics of the shear zones, since the intermediate shear axis plays a significant role in defining the orientation of the structural channels where permeability is promoted (e.g. Sibson, 2000; Rowland and Sibson, 2004; Liotta and Brogi, 2020). In particular, shear zones with a dominant transcurrent regime, such as transfer zones (Lister and Davis, 1989, Gibbs, 1990), due to their geometrical and kinematic features, can develop into relatively delimited permeable crustal volumes where magmas can be channeled, and feed shallow-level plutonic bodies, that rapidly cool down during exhumation. It is generally believed that this fast exhumation is accompanied by brittle deformation during cooling of the magmatic body (e.g. Moya et al., 2003; Liu et al., 2020). However, our analysis of the syn-tectonic Porto Azzurro pluton (Elba Island, Fig.1) shows that its exhumation is accompanied by localized ductile shear zones, developing along magmatic dykes and hydrothermal veins, involved subsequently in brittle deformation. The recognized sequence of events implies particular relationships among exhumation, cooling, stress and strain localization. To unravel the interaction between the structural history and exhumation-driven cooling, an

52 integrated approach of meso- and micro-structural studies, geochronology, thermochronology and
53 rheological modeling is here successfully applied.

54 The inner zone of the Northern Apennines (Fig. 1) represents an ideal area for investigating the above
55 described relationships, i.e. extensional structures, transfer zones (Liotta, 1991; Acocella and Funicello,
56 2006; Dini et al., 2008; Liotta and Brogi, 2020) and emplacement and exhumation of magmatic bodies
57 (Westerman et al., 2004; Dini et al., 2005; Dini et al., 2008) in a thinned continental crust (22–24 km, Di
58 Stefano et al., 2011, with references therein). This area, in fact, is affected by extensional tectonics since
59 early-middle Miocene (Carmignani et al., 1995), after having experienced thickening during the Tertiary
60 Alpine orogenesis (Carmignani et al., 2001; Molli, 2008; Rossetti et al., 2015; Bianco et al., 2019).

61 The methodological approach we applied is based on the integration of: (a) field-mapping at different
62 scales, in order to frame the (i) geometrical relationships between granitic pluton and hosting rocks, and (ii)
63 fracture network, discrete shear zones, kinematics and cross-cutting relationships; (b) micro-structural
64 studies aided by EBSD, to define the deformation temperatures on selected samples from ductile shear
65 zones; (c) geochronological and thermochronological analyses plus rheological modeling, to define the
66 timing of deformational events during exhumation.

67

68 2. Geological setting

69 Elba (Figs 1 and 2) is part of the inner zone of the Northern Apennines, an Alpine belt deriving from the
70 convergence and collision (Cretaceous-early Miocene) between Adria (a microplate, belonging to the Africa
71 plate) and the Sardinia-Corsica Massif of European pertinence (Molli, 2008 for a review; Handy et al., 2010).
72 Collision determined the stacking of oceanic and continental tectonic units deriving from the palaeo-
73 geographic domains of the Northern Apennines (Carmignani et al., 1994; Bianco et al., 2015). Since early-
74 middle Miocene, inner Northern Apennines is affected by eastwards migrating extensional tectonics that
75 consists in two main events (Brogi and Liotta, 2008; Barchi, 2010): (a) the first (early to late Miocene),
76 characterized by an extension of at least 120% (Carmignani et al., 1994; Dallmeyer, and Liotta, 1998; Brogi,
77 2006; Brogi and Liotta, 2008), gave rise to low-angle normal faults; this event produced the lateral
78 segmentation of the previously stacked tectonic units and the exhumation of mid-crustal rocks (Dallmeyer
79 and Liotta, 1998; Brogi, 2008); (b) the second (Pliocene to Present) is defined by high-angle normal faults,
80 that crosscut the previous structures (Liotta et al., 2010), and determined tectonic depressions where
81 Pliocene to Quaternary continental and marine sediments deposited (Martini and Sagri, 1993; Pascucci et
82 al., 2007; Brogi, 2011). The amount of extension related to these faults is estimated in about 6–7%
83 (Carmignani et al., 1994). The opening of the Tyrrhenian basin (Bartole, 1995; le Breton et al., 2017) and the
84 present crustal and lithospheric thicknesses, (22–24 and 30–50 km, respectively, Calcagnile and Panza, 1981;
85 Locardi and Nicolich, 1992; Di Stefano et al., 2011), are the clearest evidence of the extensional evolution.

86 Since the Langhian, the migration of extension was accompanied by magmatism, mostly of hybrid mantle-
87 crustal signature, with an eastward younging direction (Serri et al., 1993; Peccerillo, 2003). Thermal
88 perturbations related to the emplacement into the upper crust of late Miocene-Pliocene plutons, such as
89 the Porto Azzurro monzogranite (Fig. 2) at Elba (Westerman et al., 2004; Caggianelli et al., 2014), produced
90 contact metamorphic aureoles (Rossetti et al., 2007; Zucchi et al., 2017; Caggianelli et al., 2018; Pandeli et
91 al., 2018) and widespread epithermal and mesothermal mineralization through Tuscany and Elba (Dini,
92 2003) where ore deposits have been exploited for centuries. The emplacement of the Porto Azzurro Pluton
93 is interpreted as controlled by the activity of the Capoliveri-Porto Azzurro (CPA) transfer zone (Liotta et al.,
94 2015), affecting the southern part of Elba (Fig. 2).

95 Exhumation of Elba's magmatic bodies was activated in part by fault activity (Westerman et al., 2008):
96 among these, one of the most representative is the Zuccale extensional detachment fault zone (Keller and
97 Pially, 1990), well exposed at Punta Zuccale (Fig. 2), juxtaposing the Ligurian Units upon the early-middle
98 Triassic quartzite (Quarziti di Barabarca Fm., in Garfagnoli et al., 2005). The boundary is marked by a flat-
99 lying mineralized extensional shear zone, up to 5 m thick and with a top-to-the-east sense of shear,
100 regionally dipping to the East (Pertusati et al., 1993; Collettini and Holdsworth, 2004; Liotta et al., 2015).
101 Our study area is located in the footwall of the Zuccale detachment, a few tens of meters below the main
102 slip zone (Fig. 3).

103 The Porto Azzurro pluton is a coarse-grained monzogranitic body with K-feldspar megacrysts (Fig. 4), poorly
104 exposed in eastern Elba. The best outcrops are located at Capo Bianco (Marinelli, 1959), flanking the

105 Barbarossa bay (Fig. 5). The dimensions of this pluton are unknown, although gravity data (Milano et al.,
106 2019) suggest an elliptical shape within the CPA transfer zone (Liotta et al., 2015) and revealing an intrusion
107 even larger than the Monte Capanne pluton (Fig. 6), widely exposed in western Elba (Fig. 2) with diameter
108 of c. 10 km and thickness of c. 2.5 km (Farina et al., 2010).

109 The age of the Porto Azzurro monzogranite is poorly constrained. Gagnevin et al. (2011) provided in-situ U-
110 Pb zircon data for three grains yielding a weighted $^{206}\text{Pb}/^{238}\text{U}$ age of 6.53 ± 0.39 Ma. A ^{40}Ar - ^{39}Ar biotite date
111 of 5.9 ± 0.2 Ma was obtained by Maineri et al. (2003). Magma emplacement took place at pressures of 200 -
112 175 MPa, as determined from mineral assemblages in the contact aureole (Duranti et al., 1992, Caggianelli
113 et al., 2018). During magma cooling hydrothermal deposits of Fe-oxides and Fe-hydroxides formed at 5.53
114 ± 0.14 Ma (Wu et al., 2019). The wall and roof rocks (largely exposed in the Mt. Calamita promontory, Fig. 2)
115 are the structurally deepest outcropping rocks of Elba (Porto Azzurro Fm., in: Garfagnoli et al., 2005). These
116 are mainly represented by micaschist, quartzitic phyllite, quartzite and minor amphibolite levels (Barberi et
117 al., 1967; Garfagnoli et al., 2005). In the whole Mt. Calamita Promontory, and especially in the Barbarossa
118 bay, the micaschist and the monzogranite itself are injected by leucogranite dykes, quartz and tourmaline
119 veins (Fig. 7), dissected by later faults (Dini et al., 2002; Dini et al., 2008; Musumeci et al., 2011; Viti et al.,
120 2016; Zucchi et al., 2017).

121

122 3. Dataset

123 We present the collected dataset according to the planned methodological approach, finalized to
124 reconstruct the deformation and exhumation history of the pluton. In the Capo Bianco area (Fig. 5), the
125 monzogranite and its hosting rocks are structurally located in the footwall of the Zuccale extensional
126 detachment. The hosting rocks are micaschist and quartzite (see Spina et al., 2019 for information on the
127 protolith), with a well-developed schistosity, generally dipping gently westward to north-westward.
128 This schistosity is defined by low-P parageneses, generated during contact metamorphism, up to muscovite-
129 out conditions (Garfagnoli et al., 2005; Zucchi et al., 2017; Papeschi et al., 2017; Caggianelli et al., 2018)
130 producing K-feldspar + andalusite and, in quartz-free domains, K-feldspar + corundum (Fig. 4d). For the sake
131 of clarity, the data are presented in distinct sections, starting with the petrographical description of the
132 monzogranite.

133

134 3.1 Petrography of the monzogranite and felsic dykes

135 The texture of monzogranite is characterized by a coarse grain size, heterogeneous for the presence of K-
136 feldspar megacrysts up to 10 cm in length. The mineral composition includes plagioclase, K-feldspar, quartz,
137 biotite and minor white mica. Accessory phases are tourmaline, ilmenite, zircon, monazite, xenotime and
138 apatite. K-feldspar frequently shows Carlsbad twinning and perthitic exsolutions (Fig. 8a) while plagioclase
139 sometimes displays Albite-Carlsbad twinning and oscillatory zoning (Fig. 8b), reflecting the relatively fast
140 magma cooling. Quantitative SEM/EDS analyses (Appendix: Table A1 and A2) indicate that plagioclase is
141 generally zoned with andesine cores (X_{An} up to 0.39) and oligoclase rims (X_{An} down to 0.13). Biotite shows
142 a marked pleochroism with a dark brown tone and the composition is characterized by an average
143 $\text{Fe}/(\text{Fe}+\text{Mg})$ ratio of 0.56. Biotite frequently includes apatite, monazite and zircon, the latter two being
144 surrounded by sharp metamictic halos (Fig. 8c). Quartz - K-feldspar intergrowths, display micrographic
145 texture, reflecting last melt crystallization (Fig. 8d). Tourmaline is mostly of post-magmatic origin, being
146 found in veins or along thin branched fractures. The possible former presence of cordierite (Marinelli, 1959)
147 is revealed by the presence of clots made up of sericite and chlorite.

148 The felsic dykes, intruding the monzogranite and wall rocks, are medium to fine grained, and heterogeneous
149 for the presence of larger K-feldspars, up to 5 mm in length. The mineral composition includes K-feldspar,
150 plagioclase ($X_{\text{An}}=0.14-0.16$), quartz, tourmaline \pm biotite \pm white mica \pm cordierite, with accessory phases
151 represented by ilmenite, apatite, zircon and monazite. Thus, felsic dykes can be classified as tourmaline
152 leuco-monzogranite. K-feldspar displays Carlsbad twinning and perthitic exsolutions. Plagioclase is present
153 in minor amounts with respect to monzogranite and albite polysynthetic twinning is barely visible.
154 Tourmaline is generally more abundant in the felsic dykes with compared to the monzogranite. SEM/EDS
155 analyses reveal that the tourmaline can be classified as Schörl. SEM analyses on rare biotite crystals reveal
156 an elevated content in Fe with an average $\text{Fe}/(\text{Fe}+\text{Mg})$ of 0.74, distinctly higher than the value found in
157 biotite of the monzogranite. White mica \pm chlorite occur as a common product of alteration at the expense

158 of biotite, feldspars and cordierite. Late magmatic muscovite is very rare. Analysis of zircon in one sample
159 revealed an extremely high concentration of U (UO₂ up to 5.68 wt.%) that can be ascribed to disequilibrium
160 partitioning of U between crystal and melt (Wang et al., 2011).

161 The preferred orientation of the euhedral K-feldspar megacrysts in monzogranite, well visible in the field
162 (Fig. 4) and related to melt-present conditions (Paterson et al., 1989), is barely recognizable at the scale of
163 the optical microscope. In the felsic dykes, however, it can be easily recognized, even though the K-feldspars
164 are rarely euhedral, owing to subsolidus deformation.

165 166 3.2 - Structural features

167 Micaschist and monzogranite are deformed by 3 discrete faulting episodes (Fig. 5). Tourmaline is present in
168 the damage zone and along the slip-surface of the first two generations of faults, thus suggesting their
169 development in a short time interval, in the frame of a progressive deformation. The faults of the last
170 episode are without hydrothermal mineralization in their damage zones.

171 The first generation of sub-vertical faults, N-S and NNE-striking, crossed the monzogranite, the related
172 dykes and hosting rocks. Magmatic melt was channeled along these faults, resulting in decimeters-thick
173 tourmaline-rich felsic dykes. Within these dykes, a pervasive foliation, parallel to the contact with the
174 hosting rocks, is recognizable (Fig. 7). Tourmaline lineation, formed during shearing along the mylonitic
175 foliation, is more evident close to the boundary between the dykes and the hosting monzogranite (Fig. 7d).
176 Finally, cm-thick quartz-rich veins postdated the felsic dykes (Fig. 7e).

177 The second generation of faults consists of sub vertical NE-trending, left-lateral oblique-slip faults exposed
178 in the western part of the Barbarossa bay (Fig. 9a, b) and of sub-horizontal to gently E-dipping normal faults
179 (Fig. 9c). Both types of faults dissect all previous structures and are characterized by tourmaline in their
180 shear zones and by offsets ranging from few to tens of meters (Fig. 3).

181 The left-lateral oblique-slip faults are interpreted as minor faults associated to the CPA transfer zone (Fig.
182 2). The low-angle normal faults are subsidiary structures of the Zuccale normal fault (Fig. 3), affecting its
183 footwall (Liotta et al., 2015).

184 Low-angle normal faults are characterized by the presence of up to 30 cm thick mineralized cataclasite:
185 tourmaline mineralization occurs in the monzogranite (Fig. 9d), whereas graphite and tourmaline are
186 typically present in micaschist (Fig. 9e). Dilatational shear veins filled by tourmaline and subsequent Fe-
187 oxides and/or Fe-hydroxides typify the damage zone of these latter structures. Kinematic indicators are
188 given by the relationships between the tourmaline and/or graphite-bearing fault zones and associated
189 minor structures, and by mesostructures on the fault-slip plane. These latter are represented by lunate
190 structures, grooves, mega-grooves, slickenlines, quartz-fiber steps, with a top-to-the-east sense of shear,
191 defining a clear normal movement, consistent with the kinematics of the Zuccale normal fault (Pertusati et
192 al., 1993; Keller and Piali, 1990; Colletini and Holdsworth, 2004).

193 A significant low-angle normal fault characterizes the Capo Bianco promontory, and affects the roof of the
194 monzogranite (Fig. 10a,b). It defines a more than 3 m thick cataclasite level, mostly made up of comminuted
195 micaschist and monzogranite, mineralized by tourmaline and Fe-oxides and/or Fe-hydroxides. Along the
196 main slip surface a mm-thick shear vein, made up of Fe-oxides and/or Fe-hydroxides is recognizable. Along
197 this slip surface a cm-thick felsic dykelet, parallel to the shearing plane, is also hosted (Fig. 10c).
198 Furthermore, a similar dykelet is deformed in the cataclasite (Fig. 10d), indicating fault activity during dyke
199 injection. Kinematic indicators are consistent with the Zuccale detachment (Fig. 10a).

200 The occurrence of tourmaline and quartz in both NE-striking left-lateral oblique-slip faults and low-angle
201 normal faults, as well as the deposition of graphite within the cataclasite, indicates that both fault systems
202 were coeval with mineralization. The comminution of both tourmaline and quartz within the fault zones,
203 strongly suggests that the activity of both sub-vertical and sub-horizontal faults continued after the
204 mineralization event, too.

205 The third generation of faults is mostly made of NW-striking subvertical structures. These faults show up to
206 50 cm thick damage zones with shear fractures and minor faults. The cataclasite is composed of
207 comminuted rock elements, ranging in size from 0.1 to 3 cm. The angular relationships between minor
208 fractures and the main slip surfaces, together with extensional jogs (Fig. 11c), indicate a dominant right-
209 lateral shear component (Fig. 11a, b). Slickenlines on fault planes are oblique, with pitches ranging from 120°
210 to 140° (Fig. 11d, e).

211
212
213
214
215
216
217
218
219
220
221
222
223
224
225
226
227
228
229
230
231
232
233
234
235
236
237
238
239
240
241
242
243
244
245
246
247
248
249
250
251
252
253
254
255
256
257
258
259
260
261
262
263
264

3.3 Microstructural analysis

Rock samples from each structural setting were studied microstructurally. These include felsic dykes and quartz-rich hydrothermal veins, as well as the monzogranite they intruded along the first fault generation, where ductile deformation concentrated. We present EBSD data of two key samples to highlight microstructural features representative of the distinct deformation conditions.

The first sample (Fig. 7c, sample RG2) consists of a foliated felsic dyke with a maximum thickness of c. 20 cm, crosscutting the monzogranite. The dyke shows a clear mylonitic fabric with evidence of dextral extensional shear, resulting in strongly boudinaged K-feldspar (Kfs). In Fig. 12a, a boudinaged Kfs-clast with recrystallized necks and deformed tails, is enveloped by dynamically recrystallized 10 to 50 μm large quartz crystals. Plagioclase recrystallized to significantly smaller grains ($< 10 \mu\text{m}$), that is interlayered between the Kfs clasts and the quartz tails.

EBSD analysis was applied on five areas of sample RG2 to document the deformation microstructures, as well as the type of crystallographic preferred orientations (CPOs). This approach provides an insight into the activated slip systems within quartz and Kfs during plastic deformation, and allows to estimate the deformation temperatures.

Figure 12a shows that boudinaged Kfs clasts are twinned according to the Carlsbad law, and the recrystallized grains within the neck have variable misorientations.

Four of the five selected sites for quartz CPO analysis are in the Kfs-rich parts of the dyke, whereas the fifth is located in a quartz-dominated vein containing boudinaged tourmaline and few strongly deformed Kfs crystals. Figure 12b reveals that most of the recrystallized quartz grains have a reddish color and hence a strong attitude to have their c-axes aligned towards the observer. The crystallographic orientations of all quartz grains within the analyzed sites give identical indications.

Pryer (1993) suggests that Kfs plastic deformation is only expected at temperatures exceeding 600 $^{\circ}\text{C}$. We have tried to reconstruct from the EBSD map the possible slip systems that may have operated during the ductile necking of the Kfs clast. For this purpose, we have constructed a pole figure plot that considers just one analytical point for every recrystallized Kfs-grain in the neck (Fig. 13). The most likely operating slip system during Kfs boudinage was $(110)_{1/2}[1-12]$. Dispersion of the slip directions in an ill-defined girdle may suggest dislocation creep to have been accommodated by grain boundary sliding and possibly by a diffusion controlled mass transfer process. The latter is suggested by the growth of Kfs-fringes in the strain shadow of the large grey undeformed plagioclase crystal (on the lower right of the Fig. 12a), which must have been in a hard slip position.

TEM analysis of experimentally deformed Kfs crystals (Willaime et al., 1979; Scandale et al., 1983) in the temperature range between 700 and 900 $^{\circ}\text{C}$ and at strain rates of $2 \times 10^{-6} \text{sec}^{-1}$, shows that the easiest slip systems in Kfs are those with glide along the cleavage planes $(010)[001]$ and $(010)[101]$. Another possible slip system is $(110)_{1/2}[1-12]$, coherent with our data.

Deformation temperatures consistent with 600 $^{\circ}\text{C}$ are also supported by the recrystallized quartz grains. This is confirmed by the pole figures shown in Fig. 13, where quartz c-axes maxima are concentrated in the central part, and poles to a-prisms $\{11-20\}$ and m-prisms $\{10-10\}$ are aligned along the primitive great circle. Schmid and Casey (1986) have shown that in metamorphic rocks deformed at normal geological strain rates, these quartz pole figures are characteristic of the upper amphibolite facies conditions, and are consistent with temperatures of about 600 $^{\circ}\text{C}$, already suggested by the plastically deformed Kfs clasts.

Concerning the second sample (RG4), we have studied the transition between the foliated monzogranite and a tourmaline-bearing quartz-rich hydrothermal vein where an evolution from a mylonitic to ultramylonitic fabric is observed. Figure 14a shows the areas analyzed in the scanned thin section (at plane polarized light) with a closely flat running foliation in the ultramylonitic zone (Fig. 14b). In the upper third of the thin section, larger biotite flakes highlight the foliated monzogranite. In the central mylonitic part, biotite has become strongly deformed and altered. We present data from two microstructurally distinct areas (red squares, in Fig. 14a,b), that progressively accommodate increasing amounts of deformation in the mylonitic part (Fig. 15a,b), which allow us to understand the deformation mechanisms and temperature conditions affecting this micro shear zone. The CPOs of these recrystallized quartz grains will then be compared with those of sample RG4, previously described and which deformed at about 600 $^{\circ}\text{C}$.

Figure 15a, an Inverse Pole Figure (IPF) color coded orientation map, shows how quartz of the foliated monzogranite deforms when it meets the upper shear zone boundary. Large grains of the quartz layer show

265 only limited internal deformation in form of the arranged subgrain-boundaries (upper part of Fig. 15a). Grain
266 size reduction is confined to high stress zones, distinguished by fracture propagation. Here, recrystallization
267 results in a typical grain size smaller than 10 μm . The EBSD orientation map shows that recrystallized grains
268 deriving from different quartz domains mix up and assume misorientations among grains from 2° to > 60°.
269 Mixing up of recrystallized quartz grains originally belonging to distinct large quartz grains suggest that
270 grain boundary sliding has been important during this incipient deformation (Ishii et al., 2007).
271 In the central part of the mylonitic shear zone, grain size reduction of quartz is pronounced (Fig. 15b), even
272 though few larger remnant grains, showing core-mantle microstructures, are still preserved. Plots of the
273 EBSD data in pole figures (Fig. 13e) show a distribution of c-axes characteristic for a type-I crossed girdle
274 according to Lister (1981), suggesting the activation of basal <a>, rhombs <a> and prism <a> slip systems,
275 typically operating at greenschist facies conditions during metamorphism and therefore at temperatures of
276 about 450 °C. The intense strain gradient that evolved within the shear zone, resulting in complete
277 recrystallization and progressive grain size reduction towards the ultramylonitic part of the shear zone,
278 suggests a strain softening mechanism. Considering that the analyzed shear zone nucleated on a
279 tourmaline-bearing quartz-rich hydrothermal vein, it is reasonable that fluids conveyed along the vein
280 promoting strain softening. Hence, ductile deformation of the veins and adjacent monzogranite clearly
281 occurred later and at lower temperature than the deformation affecting the felsic dykes.
282

283 3.4. U-Pb geochronological data

284 After having defined deformation characteristics and their related temperatures, we now focus on the time
285 constraints by U-Pb geochronological data. Since we consider existing U-Pb SIMS analyses on only three
286 magmatic zircon grains from the Porto Azzurro monzogranite (Gagnevin et al., 2011) not robust enough
287 from a statistical point of view, we decided to analyze 79 out of 132 inspected zircon grains from two samples
288 of the monzogranite exposed in Capo Bianco promontory and La Serra locality (Fig. 2). We have analyzed
289 them with LA-ICP-MS for U-Pb zircon dating (see appendix).

290 U-Pb data were obtained for sample RG14 from the La Serra locality and sample RG12 from the Capo Bianco
291 locality (Table A3).

292 Sixty-one zircon grains were initially studied from RG14 using cathodoluminescence (CL) imaging in the
293 SEM. Zircon grains are characterized by complex internal features, with rare continuous oscillatory zoning
294 (Fig. 16a). Instead, zircon grains show usually domains or well-defined cores characterized by different CL
295 features with respect to the surrounding rims or rim-domains (Fig. 16a-d). Brighter irregular surfaces can
296 occur between these different domains (Fig. 16c, d).

297 Thirty-nine U-Pb analyses were performed on thirty-eight selected zircon grains. Spot analyses were
298 located mainly at the outer rims with oscillatory zoning. U-Pb results are mostly discordant with only seven
299 concordant data. $^{206}\text{Pb}/^{238}\text{U}$ apparent ages range from 5.6 to 7.2 Ma.

300 Seventy-two zircon grains were inspected for sample RG12 at the SEM for internal features. The images
301 revealed that zircon grains are commonly characterized by two domains with different CL features, locally
302 separated by a brighter thin domain (Fig. 16e). Oscillatory zoning is common for the external domains (Fig.
303 16e), whereas the inner portions are characterized by more complex zoning features (Fig. 16f-h). Convoluted
304 zoning is common and can locally interest entire grains (Fig. 16f, g), whereas sector zoning is less frequent
305 but occupies large portions of the zircon grains (Fig. 16h).

306 Forty U-Pb analyses were performed on thirty-nine selected zircon grains. Spot analyses were located
307 mainly at the outer rims with oscillatory zoning. U-Pb results are mostly discordant with only four
308 concordant data. $^{206}\text{Pb}/^{238}\text{U}$ apparent ages range from 5.9 to 7.9 Ma.

309 The isotopic data obtained from the two samples are predominantly discordant and the $^{206}\text{Pb}/^{238}\text{U}$ data
310 define a main peak between 6 and 7 Ma. The large occurrence of discordant data can be due to limitations
311 of the LA-ICP-MS technique, unable to detect low concentrations of ^{207}Pb in young zircon grains. Another
312 possible cause of discordance can be due to the analyses of distinct domains. Zircon shows complex zoning
313 features, clearly associated to different growth stages. Although the analyses were mainly located at the
314 outermost rims, likely associated with the last growth stage, we obtained a large age interval.

315 Combining the U-Pb data with CL images, we observed that the oldest ages (see Fig. 16h) are commonly
316 associated with zircon cores showing CL features that are different and discordant with those of the
317 surrounding thin rims, having oscillatory zoning. This observation suggests the presence of xenocrysts and

318 inherited grains, in agreement with Gagnevin et al. (2011). Thus, excluding outliers (5 on 39 and 8 on 40 data,
 319 from sample RG12 and RG14, respectively), the average ages of the two samples are 6.4 ± 0.4 Ma and $6.4 \pm$
 320 0.3 Ma (Fig. 17), respectively and very close to the Gagnevin et al. (2011) results. A similar U-Pb
 321 geochronological result was obtained from the Calamita schists, affected by contact metamorphism (LA-
 322 ICP-MS data on one zircon rim, Musumeci et al., 2011).

323

324 4. Post-emplacement thermo-rheological evolution

325 In order to constrain the deformational evolution with time of the above analyzed meso- and micro-
 326 structures, we simulated thermal and rheological evolution of the Porto Azzurro pluton for 1 Ma after its
 327 emplacement, taking into account the thermo-chronological constraints provided by zircon U-Pb and
 328 biotite Ar-Ar dating. In the following, we present the thermal and rheological evolution both in terms of
 329 static and dynamic approaches, with the aim to highlight the contribution of extensional tectonics in
 330 favoring cooling and migration of the brittle/ductile transition towards shallower structural levels.

331

332 4.1 Thermal evolution

333 The early cooling history of the Porto Azzurro monzogranite has been firstly simulated in static conditions
 334 through a unidimensional thermal model (Caggianelli et al., 2018) by numerically solving the differential
 335 equation:

336

$$\frac{\partial T}{\partial t} = \frac{K}{\rho C_p} \left(\frac{\partial^2 T}{\partial z^2} \right) + \frac{A}{\rho C_p} \quad (1)$$

337

338

339 where T , t and z are temperature, time and depth, respectively; K , ρ , C_p and A are thermal conductivity,
 340 density, specific heat and radiogenic heat production, respectively (Table 1). Crust and lithosphere
 341 thicknesses are fixed at 28 and 56 km respectively, in agreement with the supposed condition in Tuscany
 342 during late Miocene (Caggianelli et al., 2014). The pluton was assigned a tabular shape with a thickness of 3
 343 km and an initial temperature of 850 °C. The effect of latent heat for magma crystallization was considered
 344 in the temperature interval of 850-650 °C (Table 1).

345 The results obtained by a program in Stella[®] code are here proposed through a T-t diagram for the first 1
 346 Ma after magma emplacement fixed at 6.4 Ma (Fig. 18). In the same diagram, it is presented a second
 347 cooling history, ongoing dynamically during pluton unroofing at an initial rate of 5 mm/yr, decreasing
 348 exponentially according to a decay constant (c) of c. 10^{-6} yr⁻¹, similarly to the model proposed for the Monte
 349 Capanne intrusion (Caggianelli et al., 2014), reducing in 1 Ma the crust and lithosphere thicknesses to c. 25
 350 and 53 km, respectively. The second cooling history incorporates the effect of heat advection due to rock
 351 exhumation and thus the differential equation, to be solved numerically, becomes:

352

$$\frac{\partial T}{\partial t} = \frac{K}{\rho C_p} \left(\frac{\partial^2 T}{\partial z^2} \right) + \frac{A}{\rho C_p} - v_z \frac{\partial T}{\partial z} \quad (2)$$

353

354

355 with

356

$$v_z = \frac{dz}{dt} = -cz \quad (3)$$

357

358

359 A slight discrepancy between the two cooling histories is perceptible (Fig.18), once about 0.7 Ma are elapsed
 360 from the time of emplacement, since the dynamical model reproduces a slightly faster cooling rate. The
 361 available dating of zircon by U-Pb and of biotite by Ar/Ar (see section 2) were plotted on the same T-t
 362 diagram. It is assumed that zircon age corresponds to crystallization at c. 800 °C, and that biotite age
 363 corresponds to a closure temperature of 430 °C, obtainable by Dodson (1973) formula with Ar diffusion
 364 parameters by Harrison et al. (1985). It may appear that the biotite closure temperature is too high with
 365 respect to the normally adopted values (e.g. 280-345 °C in Harrison et al., 1985), but the resulting number is

366 mostly an effect of the size of the biotite laminae (width of 1-2 mm) and, above all, of the elevated cooling
367 rate (at least 150 °C/Myr) expected for the top of the shallow Porto Azzurro magmatic body. Ar diffusion in
368 biotite was recently simulated through numerical models by Skipton et al. (2018), which demonstrate that
369 at 450 °C, Ar retention in biotite is sensibly controlled by the cooling rate. Anyway, modeled cooling histories
370 are compatible with thermochronological data.

371

372 4.2 Rheological evolution

373 Numerical results of the cooling histories have been used to construct simplified rheological evolutions. For
374 the estimation of the brittle strength we used the equation by Sibson (1974):

375

$$376 \sigma = \sigma_1 - \sigma_3 = \beta(1 - \lambda)\rho gz \quad (4)$$

377

378 where σ is differential stress, β is a dimensionless parameter depending on the frictional coefficient and
379 tectonic regime and λ is the pore fluid pressure value.

380 For the estimation of the ductile strength we used the power-law dislocation creep equation (see Ranalli,
381 1995):

382

$$383 \frac{d\varepsilon}{dt} = A_c \sigma^n \exp\left(-\frac{E}{RT}\right) \quad (5)$$

384

385 where $d\varepsilon/dt$ is the strain rate, σ is differential stress, A_c , n and E are creep parameters, R is the gas constant
386 and T is the temperature.

387 Selected values are as follows: a pore fluid pressure factor (λ) of 0.9, a β value of 0.75 adequate for an
388 extensional tectonic context, and a strain rate of $1 \times 10^{-14} \text{ s}^{-1}$ during ductile deformation by dislocation creep
389 mechanism. The flow law parameters of quartzite and granite (Ranalli, 1995) have been used for roof rocks
390 and Porto Azzurro monzogranite, respectively (Table 2). Depth-strength diagrams at 300, 600 and 1000 kyr
391 are provided in Fig. 19. According to the static model, the B/D (brittle/ductile) transition at 300 kyr is in the
392 roofing rocks at $z = 5$ km, well above the contact with the underlying monzogranite, located at c. 6.4 km. At
393 600 kyr the B/D transition deepens ($z = 5.6$ km) but still remains above the wall rock - pluton contact.
394 However, the lithological change from wall rock to granite generates a passage to the brittle domain and
395 the appearance of a second B/D transition at a depth of 6.8 km. Consequently, at this time the top of the
396 pluton is already entered into the brittle domain. At 1 Myr, the shallower B/D transition disappears and the
397 deeper one drifts to a depth of 7.8 km well within the plutonic body. The dynamic model (Fig. 19b) differs in
398 producing shallower B/D transitions and in anticipating the passage to the brittle domain owing to the faster
399 cooling of the pluton and roof rocks.

400 The evolution of the B/D transitions for 1 Ma starting from magma emplacement is portrayed in the diagram
401 of Fig. 20 for both the static and dynamic conditions. In the static case, it can be seen that the minimum
402 depth of the B/D transition (c. 5 km) occurs at c. 250 kyr (point x in Fig. 20a). Instead, the genesis of the
403 second B/D transition takes place at c. 500 kyr (point z). Finally, at 900 kyr the shallower B/D transition (point
404 y) disappears and all the wall rocks pass to the brittle domain. In the dynamic case, the passage of the top
405 of the monzogranite to the brittle domain (point z in Fig. 20b) is anticipated by about 120 kyr (i.e. at c. 380
406 kyr), whereas the shallower B/D transition culminates after c. 500 kyr at a minimum depth of c. 3.6 km (point
407 x) and disappears after c. 750 kyr (point y). Afterwards, the whole plutonic body, with the exception of the
408 deepest part, migrates into the brittle domain.

409

410 5. Final exhumation: (U-Th)/He dating

411 For the sake of completing the exhumation history of the Porto Azzurro monzogranite (sample RG12), the
412 apatite He ages provide the best constraints on when the exhumation event ceased. In this view we
413 performed (U-Th)/He thermo-chronology on apatite yielding an age of 5.0 ± 0.6 Ma (for more detail see
414 Table A4, in Appendix) related to an assumed T of c. 60°C.

415 Therefore, the pluton apatite He age is 1.4 ± 0.6 Myr younger than the zircon U-Pb age, suggesting that
416 within less than 2 million years after emplacement the pluton had exhumed and cooled. It is likely that over
417 this time interval the geothermal gradient (g) was still high, as measured in geothermal areas subjected to
418 shallow magma intrusion and exhumation (e.g. Larderello, Dini et al. 2005; Taupo, Rowland and Sibson,
419 2004; Los Humeros, Prol-Ledesma and Morán-Zenteno, 2019).

420 Assuming a thermal gradient of c. 100 °C per km, an averaged exhumation rate in the order of 4.0 mm/yr is
421 possible, higher than the average value of c. 3.4 mm/yr during the first 1 Myr in the modeled cooling history.
422 This suggests an acceleration of the exhumation history in its last part.

423

424 6. Discussion

425 The meso-structural analysis, together with the kinematic study, indicate that the tectonic context in which
426 monzogranite emplacement and deformation took place is extensional. Almost vertical N- and NE-striking
427 faults and felsic dykes (i.e. first generation faults, Fig. 5), as well as low- to middle-angle normal faults
428 (second generation faults, Figs. 3 and 5) and later NW-striking oblique-slip faults (third generation faults,
429 Fig. 5) are framed in the common deformational setting of the CPA (Capoliveri-Porto Azzurro) transfer zone
430 (Fig. 2b), as already described by Liotta et al. (2015). The study area, in fact, is exactly located along the
431 transfer zone. Here, the interplay between the Zuccale extensional detachment and those structures
432 forming the transfer zone (i.e. N-, NE- and NW-striking sub-vertical oblique- to strike-slip faults) caused the
433 localized increase of the permeability, favoring the magma migration through the transfer zone and its
434 emplacement at shallow crustal level (Caggianelli et al., 2018, with references therein). Normal and strike-
435 /oblique-slip faulting assisted the magma intrusion and continued their activity also during magma cooling,
436 promoting injections of felsic dykes along sub-vertical dilatational fractures, affecting the monzogranite and
437 the hosting rocks. This is consistent with failure envelopes (Cox, 2010) favoring fracture permeability
438 development at shallow crustal levels in extensional and strike slip contexts.

439 The Zuccale detachment played the role of an unroofing fault system during magma cooling (Smith et al.,
440 2011), while the coexisting transfer faults separated crustal volumes with different amounts of extension
441 and of vertical movements (Liotta et al., 2015). It is this mechanism that controlled fast uplift of the
442 extending crust and the progressive exhumation of the magmatic bodies.

443 Fast exhumation implies two main regional factors: (i) high heat flux, promoting a decrease of rock density
444 and, (ii) relatively high extensional strain rate ($\geq 1 \times 10^{-14} \text{ s}^{-1}$, Ranalli, 1995). Since the first factor can be easily
445 linked to magma emplacement, extensional strain rate is conversely computed considering restored
446 balanced regional geological sections (Carmignani et al., 1994; Dallmeyer and Liotta, 1998), resulting in 3×10^{-14}
447 s^{-1} , during the Miocene. Locally, in Elba, even greater values can be indicated referring to the Zuccale fault
448 activity, encompassed between 7 and 5 Ma (Westerman et al., 2004; Dini et al., 2008) and resulting in a total
449 throw of 6 km (Pertusati et al., 1993). Considering these data, an average slip rate of about 3 mm/yr at least
450 can be assumed. Collettini et al. (2009) explain these relevant values considering metamorphic reactions
451 caused by fluid-rock interactions and determining talc inducing fault-weakening. In the same line, we have
452 evidence for syn-tectonic injection of lower density melt in the slip zone of the fault at the roof of the
453 monzogranite, thus promoting fault-weakening, too. A further element acting for fault weakening is
454 represented by the occurrence of graphite along the slip surfaces and within the damage zone of normal
455 faults affecting the hosting rocks (Liotta et al., 2015) and responsible for unroofing the Porto Azzurro
456 monzogranite.

457 In the time interval from 6.4 to 5 Ma, exhumation rate is determined to be between 3.4 and 3.9 mm/yr, as
458 estimated on the basis of geochronological, thermo-chronological data and on the modeling. This rate
459 exceeds the so far determined values for inland Tuscany (Balestrieri et al., 2003, 2011; Fellin et al., 2007;
460 Thomson et al., 2010; Abbate et al., 1994; Carminati et al., 1999; Coli, 1989), where the highest values (1.3 -
461 1.8 mm/yr) have been determined, on the basis of fission tracks analysis on apatite and zircon, during late
462 Miocene, after and before periods where exhumation rate is lesser than 1 mm/yr (Balestrieri et al., 2003;
463 Fellin et al., 2007; Thomson et al., 2010).

464 The difference between the Porto Azzurro exhumation rate and those reported for Tuscany, is explained by
465 the: (i) significant enhancement of lithospheric stretching and high heat flow; (ii) localized magma
466 emplacement; (iii) rapid granite unroofing, as suggested by the slip rate of Zuccale fault, and consequent
467 fast cooling rate. Significantly, this localized high exhumation occurred during an acceleration of the

468 regional exhumation documented for the late Miocene (Balestrieri et al., 2003; Fellin et al., 2007; Thomson
469 et al., 2010).

470 Reasonably, the above mentioned processes are linked to the migration of the brittle/ductile transition
471 toward shallower crustal levels, as a consequence of the thermal perturbation induced by monzogranite
472 emplacement which promoted the weakening of the upper crust. The melt and hydrothermal fluid
473 migrations caused acceleration of fault slip rates.

474 Field evidence indicates that the brittle/ductile migration was a quick event, since ductile deformational
475 features are limited to localized melt-assisted shear zones, followed by high temperature fluid flow within
476 discrete zones.

477 In fact, microstructural analysis of the felsic dyke (Fig. 7c) suggests high deformation temperatures. These
478 allowed boudinaged Kfs to recrystallize ductilely, quartz to deform by prism $\langle a \rangle$ slip and hence consistent
479 with ductile Kfs-recrystallization. Prism $\langle c \rangle$ slip at geological strain rates is typical for granulite facies
480 conditions, at temperatures higher than 650 °C (Mainprice et al., 1986), whereas prism $\langle a \rangle$ slip is consistent
481 with upper amphibolite facies conditions (Schmid and Casey, 1986) and therefore at about 600 °C.

482 The microstructural interrelationships support that deformation of the felsic dyke occurred after melt-
483 present monzogranite deformation. Strain softening due to fluid flow along the dykes will have allowed
484 faster strain rates than are typically registered during main geological deformation events, and will have
485 been in the order of $1 \times 10^{-9} \text{ s}^{-1}$ (e.g. Tullis et al., 1973; Kruhl, 1998; Okudaira et al., 1998), a value that is
486 compatible with the slip-rate of the Zuccale fault.

487 Quartz-rich hydrothermal vein sample RG₄ shows deformation microstructures formed during lower
488 temperature conditions than those preserved within sample RG₂. In sample RG₄ we have studied the
489 transition from foliated monzogranite to the tourmaline-bearing quartz-rich vein which is accompanied by
490 the evolution from a mylonitic to an ultramylonitic fabric. Figure 7e suggests that mylonitic deformation of
491 the monzogranite next to the vein, as well as of the vein itself, was triggered by fluid-induced weakening.
492 Since the dyke and vein are close to one another (just 10 meters), deformation along both discrete shear
493 zones must have occurred at different times after the monzogranite crossed the brittle-ductile transition
494 boundary during cooling and exhumation. By considering the thermo-rheological evolution depicted in
495 Figures 18 and 20b, it can be deduced that the monzogranite, close to the roof rocks, entered the brittle field
496 at 480 °C after 380 kyr had elapsed after pluton emplacement. This is a minimum estimate for the timing of
497 the dyke injection and dyke deformation, considered that a brittle behavior of the monzogranite is
498 necessary for a dyking process.

499 Quartz CPOs of the mylonitic monzogranite next to the tourmaline-bearing quartz-rich vein suggest
500 deformation temperatures of about 450 °C (Fig. 15a). This implies that hydrothermal vein deformation has
501 occurred c. 550 kyr after monzogranite emplacement (see Fig. 18). A deformation temperature difference
502 of >150 °C between the dyke and the vein is supported by the quartz pole figures that suggest rhombohedral
503 $\langle a \rangle$ slip together with basal $\langle a \rangle$ slip and subordinated prism $\langle a \rangle$ slip (Passchier and Trouw, 2005) for
504 deformation of the vein.

505 This reconstruction unveils that the fast transition into the brittle domain, still involves ductile deformation,
506 in contrast with what is expected for quickly cooling upper crustal granitic plutons (Caggianelli et al., 2000;
507 Moyen et al., 2003; de Saint-Blanquat et al., 2006; González Guillot et al., 2018; Liu et al., 2020).

508

509 **7. Conclusions**

510 The integration among meso- and microstructural analyses, geochronological, thermo-chronological
511 studies and modeling allows us to state that Porto Azzurro monzogranite emplaced, on the basis of our new
512 dataset, at 6.4 ± 0.4 Ma in the upper crust (about 6.5 km depth) in an extensional setting, within a transfer
513 zone of crustal relevance. Consequently, it experienced fast cooling and a quick transition into the brittle
514 regime. Nevertheless, this is marked by ductile deformation, within discrete melt- and fluid-assisted shear
515 zones, as highlighted by EBSD data of ductilely deformed K-feldspar and quartz.

516 The thermo-rheological model indicates that the upper part of the monzogranite entered into the brittle
517 domain c. 380 kyr after its emplacement, allowing dyke formation and melt-injection that triggered
518 localized high strain ductile deformation. The subsequent stage of ductile deformation happened at c. 170
519 kyr later, and affected quartz-rich veins at lower temperatures, most likely due to enhanced fluid-flow within
520 the localized shear zones.

521 The cooling history of the pluton developed during fast exhumation, with an estimated rate ranging from c.
522 3.4 to 4.0 mm/yr, and was promoted by transfer faults working in concert with dilational and unroofing faults
523 in the frame of the Neogene extensional tectonics.

524 The key-message of our conclusion is that ductile deformation can affect a granitic intrusion even when it is
525 already entered into the brittle domain, due to localized thermo-rheological perturbations, caused by late
526 magmatic and hydrothermal events, in an extensional regime.

527

528 Acknowledgments

529 We acknowledge Andrea Dini for the discussion on the Elba magmatism and for its guidance in the main
530 outcrops described in this paper. We gratefully thank an anonymous referee for his/her very constructive
531 suggestions and comments that significantly improved the manuscript. We also warmly thank the editor
532 Joao Hippertt for handling our manuscript and his helpful advises. A.B, A.C., C.B., D.L., M.Z. received
533 funding from the European Community's Seventh Framework Programme under grant agreement No.
534 608553 (Project IMAGE). R.S thanks the grants DOR1827303 of the University of Padova and of Italian PRIN
535 20178LPCP.

536

537

538

539 References

540 Abbate, E., Balestrieri, M.L., Bigazzi, G., Norelli P., Quercioli, C., 1994. Fission-track datings and recent
541 rapid denudation in northern Apennines, Italy. *Mem. Soc. Geol. Ital.* 48, 579-585.

542 Acocella, V., Funicello, R., 2006. Transverse systems along the extensional Tyrrhenian margin of central
543 Italy and their influence on volcanism. *Tectonics* 25. <http://dx.doi.org/10.1029/2005TC001845>.

544 Balestrieri, M.L., Bernet, M., Brandon, M.T., Picotti, V., Reiners, P., Zattin, M., 2003. Pliocene and
545 Pleistocene exhumation and uplift of two key areas of the northern Apennines: Quaternary
546 International 101, 67-73. doi: 10.1016/S1040-6182(02)00089-7.

547 Balestrieri, M.L., Pandeli, E., Bigazzi, G., Carosi, R., Montomoli, C., 2011. Age and temperature constraints
548 on metamorphism and exhumation of the syn-orogenic metamorphic complexes of Northern
549 Apennines, Italy. *Tectonophysics* 509, 254-271.

550 Barberi, F., Brandi, G.P., Giglia, G., Innocenti, F., Marinelli, G., Raggi, R., Ricci, C.A., Squarci, P., Taffi, L.,
551 Trevisan, L., 1967. Carta Geologica dell'Isola d'Elba alla scala 1:25.000. E.I.R.A., Firenze.

552 Barchi, M.R., 2010. The Neogene-Quaternary evolution of the Northern Apennines: crustal structure, style
553 of deformation and seismicity. In: Beltrando, M., Peccerillo, A., Mattei, M., Conticelli, S., Doglioni, C.
554 (Eds.), *The Neogene-Quaternary Evolution of the Northern Apennines: Crustal Structure, Style of*
555 *Deformation, Seismicity.* *Journal of the Virtual Explorer* 36, 10pp. <http://dx.doi.org/10.3809/jvirtex.2009.00220>.

557 Bartole, R., 1995. The North Tyrrhenian-Northern Apennines post-collisional system: constraints for a
558 geodynamic model. *Terra Nova* 7, 7-30.

559 Bianco, C., Brogi, A., Caggianelli, A., Giorgetti, G., Liotta, D., Meccheri, M., 2015. HP-LT metamorphism in
560 Elba Island: Implications for the geodynamic evolution of the inner Northern Apennines (Italy).
561 *Journal of Geodynamics* 91, 13-25.

562 Bianco, C., Godard, G., Halton, A., Brogi, A., Liotta, D., Caggianelli, A., 2019. The lawsonite-glaucophane
563 blueschists of Elba Island (Italy). *Lithos* 348-349, 105198. <https://doi.org/10.1016/j.lithos.2019.105198>

564 Brogi, A., 2006. Neogene extension in the Northern Apennines (Italy): insights from the southern part of
565 the Mt. Amiata geothermal area. *Geodinamica Acta* 19, 33-50.

566 Brogi, A., 2008. Kinematics and geometry of Miocene low-angle detachments and exhumation of the
567 metamorphic units in the hinterland of the Northern Apennines (Italy). *Journal of Structural Geology*
568 30, 2-20.

569 Brogi, A., 2011. Bowl-shaped basin related to low-angle detachment during continental extension: the case
570 of the controversial Neogene Siena Basin (central Italy, Northern Apennines). *Tectonophysics* 499,
571 54-76.

- 572 Brogi, A., Liotta, D., 2008. Highly extended terrains, lateral segmentation of the substratum, and basin
573 development: the Middle-Late Miocene Radicondoli Basin (inner northern Apennines, Italy).
574 *Tectonics* 27, <http://dx.doi.org/10.1029/2007TC002188> TC 5002.
- 575 Caggianelli, A., Prosser, G., & Rottura, A. (2000). Thermal history vs. fabric anisotropy in granitoids
576 emplaced at different crustal levels: an example from Calabria, southern Italy. *Terra Nova*, 12(3), 109-
577 116. doi:10.1046/j.1365-3121.2000.123280.x
- 578 Caggianelli, A., Ranalli, G., Lavecchia, A., Liotta, D., Dini, A., 2014. Post-emplacement thermo-rheological
579 history of a granite intrusion and surrounding rocks: the Monte Capanne pluton, Elba Island, Italy. In:
580 In: Llan-Fúnez, S., Marcos, A., Bastida, F. (Eds.), *Deformation Structures and Processes Within the*
581 *Continental Crust*. Geological Society, London, Special Publication 394, 129-143.
- 582 Caggianelli, A., Zucchi, M., Bianco, C., Brogi, A., Liotta, L., 2018. Estimating P-T metamorphic conditions
583 on the roof of a hidden granitic pluton: an example from the Mt. Calamita promontory (Elba Island,
584 Italy). *Italian Journal of Geosciences* 137, 238-253.
- 585 Calcagnile, G., Panza, G.F., 1980. The main characteristics of the Lithosphere Asthenosphere System in
586 Italy and surrounding regions. *Pure and Applied Geophysics* 119, 865-879.
- 587 Carmignani, L., Decandia, F.A., Disperati, L., Fantozzi, P.L., Kligfield, R., Lazzarotto, A., Liotta, D.,
588 Meccheri, M., 2001. Inner Northern Apennines. In: Vai, G.B., Martini, I.P. (Eds.), *Anatomy of an*
589 *Orogen: the Apennines and Adjacent Mediterranean Basins*, 197-213. Springer, Dordrecht.
590 https://doi.org/10.1007/978-94-015-9829-3_14
- 591 Carmignani, L., Decandia, F.A., Disperati, L., Fantozzi, P.L., Lazzarotto, A., Liotta, D., Meccheri, M., 1994.
592 Tertiary extensional tectonics in Tuscany (Northern Apennines, Italy). *Tectonophysics* 238, 295-315.
- 593 Carmignani, L., Decandia, F.A., Disperati, L., Fantozzi, P.L., Lazzarotto, A., Liotta, D., Oggiano, G., 1995.
594 Relationships between the Tertiary structural evolution of the Sardinia-Corsica-Provençal Domain
595 and the Northern Apennines. *TerraNova* 7, 128-137.
- 596 Carminati, E., Giunghi, C., Argnani, A., Sabadini, R., Fernandez, M., 1999. Plio-Quaternary vertical motion
597 of the Northern Apennines: Insights from dynamic modeling. *Tectonics* 18 (4), 703-718.
- 598 Coli, M., 1989. Time and mode of uplift of the Apuane Alps metamorphic complex. *Atti Ticinesi Scienze*
599 *della Terra* 32, 47-56.
- 600 Collettini, C., Holdsworth, R.E., 2004. Fault zone weakening processes along low-angle normal faults:
601 insights from the Zuccale Fault, Isle of Elba, Italy. *Journal of the Geological Society* 161, 1039-1052.
- 602 Collettini, C., Niemeijer, A., Viti, C., Marone, C., 2009. Fault zone fabric and fault weakness. *Nature*, Vol
603 462/17, 907-911
- 604 Cox, S.F., 2010. The application of failure mode diagrams for exploring the roles of fluid pressure and stress
605 states in controlling styles of fracture-controlled permeability enhancement in faults and shear zones.
606 *Geofluids*, 10, 217-233. doi: 10.1111/j.1468-8123.2010.00281.x
- 607 Cruden, A.R., 1998. On the emplacement of tabular granites. *Journal of the Geological Society* 155, 853-
608 862.
- 609 Cruden, A.R., 2006. Emplacement and growth of plutons: implications for rates of melting and mass
610 transfer in continental crust. In M. Brown, & T. Rushmer (Eds.), *Evolution and Differentiation of the*
611 *Continental Crust*. Cambridge UK: Cambridge University Press, 455-519.
- 612 Dallmeyer, R.D., Liotta, D., 1998. Extension, uplift of rocks cooling ages in thinned continental provinces:
613 the Larderello geothermal area (inner Northern Apennines, Italy). *Geological Magazine* 135, 193-202.
- 614 de Saint-Blanquat, M., Habert, G., Horsman, E., Morgan, S.S., Tikoff, B., Launeau P., Gleizes, G., 2006.
615 Mechanism and duration of non-tectonically assisted magma emplacement in the upper crust: The
616 Black Mesa pluton, Henry Mountains, Utah. *Tectonophysics* 428, 1-31.
- 617 Di Stefano, R., Bianchi, I., Ciaccio, M.G., Carrara, G., Kissling, E., 2011. Three-dimensional Moho
618 topography in Italy: New constraints from receiver functions and controlled source seismology.
619 *Geochemistry, Geophysics, Geosystems* 12 (9), 1-15.
- 620 Dini, A., 2003. Ore deposits, industrial minerals and geothermal resources. *Per. Mineral.* 72, 41-52.
- 621 Dini, A., Gianelli, G., Puxeddu, M., Ruggieri, G., 2005. Origin and evolution of Pliocene-Pleistocene granites
622 from the Larderello geothermal field (Tuscan Magmatic Province, Italy). *Lithos* 81, 1-31.

- 623 Dini, A., Innocenti, F., Rocchi, S., Tonarini, S., Westerman, D.S., 2002. The magmatic evolution of the Late
624 Miocene laccolith-pluton-dyke granitic complex of Elba Island Italy. *Geological Magazine* 139, 257-
625 279.
- 626 Dini, A., Westerman, D.S., Innocenti, F., Rocchi, S., 2008. Magma emplacement in a transfer zone: the
627 Miocene mafic Orano dyke swarm of Elba Island, Tuscany, Italy. *Geological Society of London Special
628 Publications* 302, 131-148.
- 629 Dodson, M.H., 1973. Closure temperature in geochronological and petrological systems. *Contributions to
630 Mineralogy and Petrology* 40, 259-274.
- 631 Duranti, S., Palmeri, R., Pertusati, P.C., Ricci, C.A., 1992. Geological evolution and metamorphic petrology
632 of the basal sequences of Eastern Elba (Complex II). *Acta Vulca. Mar.* 2, 213-229.
- 633 Farina, F., Dini, A., Innocenti, F., Rocchi, S., Westerman, D.S., 2010. Rapid incremental assembly of the
634 Monte Capanne pluton (Elba Island, Tuscany) by downward stacking of magma sheets. *Geological
635 Society of America Bulletin* 122, 1463-1479.
- 636 Farley, K.A., 2002. (U-Th)/He dating: techniques, calibrations, and applications. *Rev. Mineral. Geochem.*
637 47, 819-844. <http://dx.doi.org/10.2138/rmg.2002.47.18>.
- 638 Fellin, M.G., Reiners, P.W., Brandon, M.T., Wüthrich, E., Balestrieri, M.L., Molli, G., 2007.
639 Thermochronologic evidence for the exhumational history of the Alpi Apuane metamorphic core
640 complex, northern Apennines, Italy. *Tectonics* 26, TC6015 1-22. doi: 10.1029/2006TC002085.
- 641 Foeken, J.P.T., Persano, C., Stuart, F.M., ter Voorde, M., 2007. Role of topography in isotherm perturbation:
642 Apatite (U-Th)/He and fission track results from the Malta tunnel, Tauern Window, Austria. *Tectonics*
643 26, TC3006. doi:10.1029/2006TC002049,
- 644 Foeken, J.P.T., Stuart, F.M., Dobson, K.J., Persano, C., Vilbert, D., 2006. A diode laser system for heating
645 minerals for (U-Th)/He chronometry. *Geochemistry Geophysics Geosystems* 7 Q04015, 1-9.
646 <http://dx.doi.org/10.1029/2005GC001190>.
- 647 Gagnevin, D., Daly, J.S., Horstwood, M.S.A., Whitehouse, M.J., 2011. In-situ zircon U-Pb, oxygen and
648 hafnium isotopic evidence for magma mixing and mantle metasomatism in the Tuscan Magmatic
649 Province, Italy. *Earth and Planetary Science Letters* 305, 45-56.
- 650 Garfagnoli, F., Menna, F., Pandeli, E., Principi, G., 2005. The Porto Azzurro Unit (Mt. Calamita promontory,
651 south-eastern Elba Island, Tuscany): stratigraphic, tectonic and metamorphic evolution. *Boll. Soc.
652 Geol. Ital.* 3, 119-138.
- 653 Gibbs, A.D., 1990. Linked fault families in basin formation. *Journal of Structural Geology* 12, 795-803.
- 654 González Guillot, M., Ghiglione M., Escayola M., Martins Pimentel, M., Mortensen, J., Acevedo, R., 2018.
655 Ushuaia pluton: Magma diversification, emplacement and relation with regional tectonics in the
656 southernmost Andes. *Journal of South American Earth Sciences* 88, 497-519.
- 657 Handy, M.R., Schmid, S.M., Bousquet, R., Kissling, E., Bernoulli, D., 2010. Reconciling plate-tectonic
658 reconstructions of Alpine Tethys with the geological-geophysical record of spreading and subduction
659 in the Alps. *Earth-Science Review* 102 (3-4), 121-158.
- 660 Harrison, T.M., Duncan, I., McDougall, I., 1985. Diffusion of ⁴⁰Ar in biotite: temperature, pressure and
661 compositional effects. *Geochimica et Cosmochimica Acta* 49, 2461-2468.
- 662 Hiess, J., Condon, D.J., McLean, N., Noble, S.R., 2012. ²³⁸U/²³⁵U systematics in terrestrial uranium-bearing
663 minerals. *Science* 335 (6076), 1610-1614.
- 664 Horstwood, M.S., Foster, G.L., Parrish, R.R., Noble, S.R., Nowell, G.M., 2003. Common-Pb corrected in situ
665 U-Pb accessory mineral geochronology by LA-MC-ICP-MS. *Journal of Analytical Atomic
666 Spectrometry* 18, 837-846. doi:10.1039/B304365G.
- 667 Ishii, K., Kanagawa, K., Shigematsu, N., Okudaira, T., 2007. High ductility of K-feldspar and development
668 of granitic banded ultramylonite in the Ryoke metamorphic belt, SW Japan. *Journal of Structural
669 Geology* 29, 1083-1098. <https://doi.org/10.1016/j.jsg.2007.02.008>.
- 670 Jackson, S.E., Pearson, N.J., Griffin, W.L., Belousova, E.A., 2004. The application of laser ablation-
671 inductively coupled plasma-mass spectrometry to in situ U-Pb zircon geochronology. *Chemical
672 Geology* 211(1-2), 47-69. doi:10.1016/j.chemgeo.2004.06.017.

673 Jolivet, L., Faccenna, C., Goffé, B., Mattei, M., Rossetti, F., Brunet, C., Storti, F., Funiciello, R., Cadet, J.P.,
674 D'Agostino, N., Parra, T., 1998. Midcrustal shear zones in postorogenic extension: Example from the
675 northern Tyrrhenian Sea. *Journal of Geophysical Research* 103, 12123-12160.

676 Keller, J.V.A., Piali, G., 1990. Tectonics of the Island of Elba: a reappraisal. *Boll. Soc. Geol. Ital.* 109, 413-
677 425.

678 Kruhl, J.H., 1998. Reply. Prism- and basal-plane parallel subgrain boundaries in quartz: a microstructural
679 geothermobarometer. *Journal of Metamorphic Geology* 16, 141-146.

680 Le Breton, E., Handy, M.R., Molli, G., Ustaszewski, K., 2017. Post-20 Ma Motion of the Adriatic Plate: New
681 Constraints From Surrounding Orogens and Implications for Crust-Mantle Decoupling. *Tectonics* 36
682 (12), 3135-3154.

683 Liotta D., Brogi, A., 2020. Pliocene-Quaternary fault kinematics in the Larderello geothermal area (Italy):
684 Insights for the interpretation of the present stress field. *Geothermics* 83, 101714
685 <https://doi.org/10.1016/j.geothermics.2019.101714>

686 Liotta, D., Brogi, A., Meccheri, M., Dini, A., Bianco, C., Ruggieri, G., 2015. Coexistence of low-angle normal
687 and high-angle strike- to oblique-slip faults during Late Miocene mineralization in eastern Elba Island
688 (Italy). *Tectonophysics* 660, 17-34.

689 Liotta, D., Cernobori, L., Nicolich, R., 1998. Restricted rifting and its coexistence with compressional
690 structures: results from the Cropo3 traverse (Northern Apennines Italy). *Terra Nova* 10, 16-20.

691 Liotta, D., Ruggieri, G., Brogi, A., Fulignati, P., Dini, A., Nardini, I., 2010. Migration of geothermal fluids in
692 extensional terrains: the ore deposits of the Boccheggiano- Montieri area (southern Tuscany, Italy).
693 *Int. J. Earth Sci.* 99, 623-644.

694 Lister, G.S., 1981. The effect of basal-prism mechanism switch on fabric development during plastic
695 deformation of quartzite. *Journal of Structural Geology* 3, 67-75.

696 Lister, G.S., Davis, G.A., 1989. The origin of metamorphic core complexes and detachment faults formed
697 during Tertiary continental extension in the northern Colorado River region, U.S.A. *Journal of*
698 *Structural Geology* 11, 65-94.

699 Liu, H., Chen, Y., Wang, B., Faure, M., Erdmann, S., Martelet, G., Scaillet, B., Huang, F., 2020. Role of
700 inherited structure on granite emplacement: An example from the Late Jurassic Shibe pluton in the
701 Wuyishan area (South China) and its tectonic implications. *Tectonophysics* 779, 228394
702 <https://doi.org/10.1016/j.tecto.2020.228394>

703 Locardi, E., Nicolich, R., 1992. Geodinamica del Tirreno e dell'Appennino centro-meridionale: la nuova
704 carta della Moho. *Mem. Soc. Geol. It.* 41, 121-140.

705 Ludwig, K.R., 2003. User's Manual for Isoplot 3.00: A Geochronological Toolkit for Microsoft Excel. Kenneth
706 R. Ludwig, Berkeley Geochronology Center, Spec. Publ. 4, 74 pp.

707 Maineri, C., Benvenuti, M., Costagliola, P., Dini, A., Lattanzi, P., Ruggieri, G., Villa, I., 2003. Sericitic
708 alteration at the La Crocetta deposit (Elba Island, Italy): interplay between magmatism, tectonics and
709 hydrothermal activity. *Mineralium Deposita* 38, 67-86.

710 Mainprice, D., Bouchez, J-L, Blumenfeld, Ph, Tubià, J.M., 1986. Dominant c slip in naturally deformed
711 quartz: Implications for dramatic plastic softening at high temperatures. *Geology* 14, 819-822.

712 Marinelli, G., 1959. Le intrusioni terziarie dell'isola d'Elba. *Atti Soc. Toscana Sci. Nat. Pisa, Mem, Ser A*
713 *LXVI(I):* 50-253.

714 Martini, I.P., Sagri, M., 1993. Tectono-sedimentary characteristics of Late Miocene-Quaternary
715 extensional basins of the Northern Apennines, Italy. *Earth-Science Reviews* 34, 197-233.

716 Meesters A.G.C.A., Dunai, T.J., 2002. Solving the production-diffusion equation for finite diffusion
717 domains of various shapes: Part I. Implications for low-temperature (U-Th)/He thermochronology.
718 *Chemical Geology* 186 (3-4), 333-344.

719 Milano, M., Pierri, I., Florio, G., Cella, F., Fedi, M., 2019. Bouguer gravity field of the Tuscan Archipelago
720 (central Italy). *Journal of Maps* 15:2, 751-758. DOI: 10.1080/17445647.2019.1669499

721 Molli, G., 2008. Northern Apennine-Corsica orogenic system: an updated overview. *Geological Society,*
722 *London, Special Publications* 298, 413-442.

723 Moyen, J-F., Martin, H., Jayananda, M., Auvray B., 2003. Late Archaean granites: a typology based on the
724 Dharwar Craton (India). *Precambrian Research* 127, 103-123.

- 725 Musumeci, G., Mazzarini, F., Tiepolo, M., Di Vincenzo, G., 2011. U–Pb and ⁴⁰Ar–³⁹Ar geochronology of
726 Palaeozoic units in the Northern Apennines: determining protolith age and alpine evolution using the
727 Calamita Schist and Ortano Porphyroids. *Geological Journal* 46, 288-310.
- 728 Okudaira, T., Takeshita, T., Toriumi, M., 1998. Prism- and basal-plane parallel subgrain boundaries in
729 quartz: a microstructural geothermobarometer. *Discussion, Journal of Metamorphic Geology* 16, 141-
730 146.
- 731 Pandeli, E., Giusti, R., Elter, F.M., Orlando, A., Orti, L., 2018. Structural setting and metamorphic evolution
732 of a contact aureole: the example of the Mt. Capanne pluton (Elba Island, Tuscany, Italy). *Ofiliti* 43,
733 41-73.
- 734 Papeschi, S., Musumeci, G., Mazzarini, F., 2017. Heterogeneous brittle-ductile deformation at shallow
735 crustal levels under high thermal conditions: The case of a syn-kinematic contact aureole in the inner
736 northern Apennines, southeastern Elba Island, Italy. *Tectonophysics* 717, 547-564.
- 737 Pascucci, V., Martini, I.P., Sagri, M., Sandrelli, F., 2007. Effects of transverse structural lineaments on the
738 Neogene-Quaternary basins of Tuscany (inner Northern Apennines, Italy). In: Nichols, G., Williams,
739 E., Paola, C. (Eds.). *Sedimentary processes, Environments and Basins: a tribute to Peter Friend*. Intern.
740 Ass. Sediment., Spec. Publ. 38, 155-182.
- 741 Passchier, C.W., Trouw, R.A.J., 2005. *Microtectonics*. 2nd Revised and Enlarged Edition, 366 pp. Springer
742 Verlag.
- 743 Paterson, J.W., Newton, R.C., 1989. Reversed experiments on Biotite-Quartz-Feldspar melting in the
744 system K₂MgSi₂O₆: implication for crustal anatexis. *The Journal of Geology* 97(4), 465-485.
- 745 Peccerillo, A., 2003. Plio-quaternary magmatism in Italy. *Episodes* 26, 222-226.
- 746 Pertusati, P.C., Raggi, G., Ricci, C.A., Duranti, S., Palmeri, R., 1993. Evoluzione post-collisionale dell'Elba
747 centro-orientale. *Mem. Soc. Geol. Ital.* 49, 297-312.
- 748 Prol-Ledesma, R. M., & Morán-Zenteno, D. J. (2019). Heat flow and geothermal provinces in Mexico.
749 *Geothermics*, 78, 183–200. <http://doi.org/10.1016/j.geothermics.2018.12.009>
- 750 Pryer, L.L., 1993. Microstructures in feldspars from a major crustal thrust zone: The Grenville Front,
751 Ontario, Canada. *Journal of Structural Geology* 15(1), 21-36.
- 752 Ranalli, G., 1995. *Rheology of the Earth*. Chapman and Hall, 2nd Edition, pp 413.
- 753 Rey, P.F., Teyssier, C., Whitney, D.L., 2009. Extension rates, crustal melting, and core complex dynamics.
754 *Geological Society of America* 37(5), 391-394.
- 755 Rossetti, F., Glodny, J., Theye, T., Maggi, M., 2015. Pressure-temperature-deformation-time of the ductile
756 Alpine shearing in Corsica: From orogenic construction to collapse. *Lithos* 218-219, 99-116.
- 757 Rossetti F., Tecce F., Billi A. & Brilli M. (2007) - Patterns of fluid flow in the contact aureole of the late
758 Miocene Monte Capanne pluton (Elba Island, Italy). *The role of structures and rheology: Contrib.*
759 *Mineral. Petr.*, 153, 743-760.
- 760 Rowland, J.V., Sibson, R.H., 2004. Structural controls on hydrothermal
761 flow in a segmented rift system Taupo Volcanic Zone, New Zealand. *Geofluids* 4, 259-283.
- 762 Saint-Blanquat, M. de, Law, R.D., Bouchez, J-L., Morgan, S., 2001. Internal structure and emplacement of
763 the Papoose Flat pluton: An integrated structural, petrographic, and magnetic susceptibility study.
764 *Geological Society of American Bulletin* 113(8), 976-995.
- 765 Scandale, E., Gandais, M., Willaime, C., 1983. Transmission electron microscopy study of experimentally
766 deformed K-feldspar single crystals. The (010)[001], (001)1/2 [-112] and (1-11)1/2 [110] slip systems.
767 *Phys Chem Minerals* 9, 182-187.
- 768 Schmid, S.M., Casey, M., 1986. Complete fabric analysis of some commonly observed c-axis patterns.
769 *Mineral and Rock Deformation: Laboratory Studies - The Paterson Volume*. Geophysical Monograph
770 36, 263-286.
- 771 Smith, S.A.F., Holdsworth, R.E., Collettini, R.E., 2010. Interactions between plutonism and low-angle
772 normal faults in the upper crust: insights from the Island of Elba, Italy. *Geol. Soc. Am. Bull.* 123, 329–
773 346.
- 774 Serri, G., Innocenti, F., Manetti, P., 1993. Geochemical and petrological evidence of the subduction of
775 delaminated Adriatic continental lithosphere in the genesis of the Neogene-Quaternary magmatism
776 of central Italy. *Tectonophysics* 223, 117-214.
- 777 Sibson, R.H., 1974. Frictional constraints on thrust, wrench and normal faults. *Nature* 249, 542-544.

- 777 Sibson, R.H., 2000. Fluid involvement in normal faulting. *Journal of Geodynamics* 29, 469-499.
- 778 Skipton, D.R., Warren, C.J., Hanke, F., 2018. Numerical modeling of P-T, time and grain-size controls on Ar
- 779 diffusion in biotite: an aide to interpreting $^{40}\text{Ar}/^{39}\text{Ar}$ ages. *Chemical Geology* 496, 14-24.
- 780 Spina, A., Capezzuoli E., Brogi, A., Cirilli S., Liotta, D., 2019. Mid- to late Permian microfloristic evidence in
- 781 the metamorphic successions of Northern Apennines: insights for age-constraining and
- 782 palaeogeographical correlations. *Journal of the Geological Society* 176(6), 1262-1272.
- 783 <https://doi.org/10.1144/jgs2018-202>.
- 784 Stevenson, C.T.E., Owens, W.H., Hutton, D.H.W., Hood, D.N., Meighan, I.G., 2007. Laccolithic, as opposed
- 785 to cauldron subsidence, emplacement of the Eastern Mourne pluton, N. Ireland: Evidence from
- 786 anisotropy of magnetic susceptibility. *Journal of the Geological Society* 164, 99-110.
- 787 Thomson, S.N., Brandon, M.T., Reiners, P.W., Zattin, M., Isaacson, P.J., Balestrieri, M.L., 2010.
- 788 Thermochronologic evidence for orogen-parallel variability in wedge kinematics during extending
- 789 convergent orogenesis of the northern Apennines, Italy. *GSA Bulletin* 122, 1160-1179.
- 790 Tullis, J., Christie, J.M., Griggs, D.T., 1973. Microstructures and preferred orientations of experimentally
- 791 deformed quartzites. *Geological Society of American Bulletin* 84, 297-314.
- 792 Van Achterbergh, E., Ryan, C.G., Jackson, S.E., Griffin, W.L., 2001. Data reduction software for LA-ICP-MS.
- 793 Laser-Ablation-ICPMS in the earth sciences-Principles and applications, *Miner. Assoc. Can.* 29, 239-
- 794 243.
- 795 Vermeesch, P., 2018. IsoplotR: A free and open toolbox for geochronology. *Geoscience Frontiers* 9, 1479-
- 796 1493. doi:10.1016/j.gsf.2018.04.001.
- 797 Viti, C., Brogi, A., Liotta, D., Mugnaioli, E., Spiess, R., Dini, A., Zucchi, M., Vannuccini, G., 2016. Seismic slip
- 798 recorded in tourmaline fault mirrors from Elba Island (Italy). *Journal of Structural Geology* 86, 1-12.
- 799 Wang, X., Griffin, W.L., Chen, J., Huang, P., & Li, X. (2011). U and Th contents and Th/U ratios of zircon in
- 800 felsic and mafic magmatic rocks: improved zircon-melt distribution coefficients. *Acta Geologica*
- 801 *Sinica*, 85, 164-174. doi:10.1111/j.1755-6724.2011.00387.x.
- 802 Westerman, D.S., Dini, A., Innocenti, F., Rocchi, S., 2004. Rise and fall of a nested Christmas-tree laccolith
- 803 complex, Elba Island, Italy. In: Breitkreuz, C., Petford, N. (Eds.), *Physical Geology of High-level*
- 804 *Magmatic Systems*, Geol. Soc., London, Spec. Publ. 234, 195-213.
- 805 Widenbeck, M., Alle, P., Corfu, F., Griffin, W.L., Meier, M., Ober, F., Von Quant, A., Roddick, J.C., Spiegel,
- 806 J., 1995. Three natural zircon standards for U-Th-Pb, Lu-Hf, trace element and REE analysis.
- 807 *Geostandard Newsletter* 19, 1-23.
- 808 Willaime, Ch., Christie, J.M., Kovacs, M-P., 1979. Experimental deformation of K-feldspar single crystals.
- 809 *Bulletin de Minéralogie* 102, 168-177.
- 810 Wu, L.-Y; Stuart, F.M., Di Nicola, L., Heizler, M., Benvenuti, M., Hu, R.-Z., 2019. Multi-aliquot method for
- 811 determining (U+Th)/He ages of hydrothermal hematite: Returning to Elba. *Chemical Geology* 504
- 812 (2019) 151–157.
- 813 Zucchi, M., 2020. Faults controlling geothermal fluid flow in low permeability rock volumes: an example
- 814 from the exhumed geothermal system of eastern Elba Island (northern Tyrrhenian Sea, Italy).
- 815 *Geothermics* 85, 101765. <https://doi.org/10.1016/j.geothermics.2019.101765>.
- 816 Zucchi, M., Brogi, A., Liotta, D., Rimondi, V., Ruggieri, G., Montegrossi, G., Caggianelli, A., Dini, A., 2017.
- 817 Permeability and hydraulic conductivity of faulted micaschist in the eastern Elba Island exhumed
- 818 geothermal system (Tyrrhenian sea, Italy): insights from Cala Stagnone. *Geothermics* 70, 125-145.
- 819

820 Appendix: Analytical methods

821 During this investigation we used scanning electron microscope (SEM) for: (i) quantitative chemical analysis;

822 (ii) electron backscattered diffraction (EBSD) analysis; (iii) backscattered electron (BSE) imaging, and (iv)

823 CL-imaging; by using: an EVO Zeiss SEM at Bari University; a CamScan 2500 SEM equipped with EDX and

824 NordlyseNano EBSD detectors at University of Padova; and, a Philips XL30 electron microscope equipped

825 with a Centaurus CL detector at Pavia CNR-IGG-UOS, respectively. In situ zircon U-Pb geochronology was

826 determined by LA-ICP-MS at CNR-IGG-UOS of Pavia.

827 In situ U-Pb geochronology was determined by excimer LA-ICP-MS at CNR-IGG-UOS of Pavia. Zircons were

828 separated by conventional methods (crushing, heavy liquids, hand picking) from two samples (RG12; RG14).

829 Prior to age determination, the internal structure of the zircon grains was investigated with backscattered

830 electron (BSE) and Cathodoluminescence (CL) images using a Philips XL30 electron microscope equipped
831 with a Centaurus CL detector. Images were obtained using 15 kV acceleration and a working distance of 26
832 mm.

833 Age determinations were performed using a 193 nm ArF excimer laser microprobe (GeoLas200QMicrolas)
834 coupled to a magnetic sector ICP-MS (Element 1 from ThermoFinnigan). Analyses were carried out in single
835 spot mode and with a spot size fixed at 25 μ m. The laser was operated with a frequency of 5 Hz, and with a
836 fluence of 8 J/cm². Sixty seconds of background signal and at least 30 s of ablation signal were acquired. The
837 signals of masses 202Hg, 204(PbHg), 206Pb, 207Pb, 208Pb, 232Th, and 238U were acquired in magnetic
838 scan mode. 235U is calculated from 238U based on the mean ratio 238U/235U of 137.818, as recently
839 proposed by Hiess et al. (2012). The 202 and 204 masses were collected in order to monitor the presence of
840 common Pb in zircon. Mass bias and laser-induced fractionation were corrected by adopting external
841 standards, the GJ-1 zircon standard (608.56 \pm 0.4 Ma; Jackson et al., 2004). During an analytical run of zircon
842 analyses, a reference zircon 91500 (Wiedenbeck et al., 1995) was analyzed together with unknowns for quality
843 control. Data reduction was carried out through the GLITTER software package (Van Achterbergh et al.,
844 2001). Time-resolved signals were carefully inspected to detect perturbation of the signal related to
845 inclusions, cracks, or mixed-age domains. Within the same analytical run, the error associated with the
846 reproducibility of the external standards was propagated to each analysis of sample (see Horstwood et al.,
847 2003), and after this procedure each age determination was retained as accurate within the quoted error.
848 The Concordia test was performed for each analytical spot from 206Pb/238U and 207Pb/235U ratios using
849 the function in the software package Isoplot/Ex 3.00 [Ludwig, 2003]. Percentage of discordance has been
850 calculated as $\{[1 - (206\text{Pb}/238\text{U age}/207\text{Pb}/235\text{U age})] \times 100\}$. Errors in the text and figures are reported as
851 2sigma. The IsoplotR software (Vermeesch, 2018) was used to draw diagrams of age data. U-Pb isotope
852 analyses and calculated ages of zircons are reported in the data repository (Table A3).

853 Single crystal apatite (U-Th)/He dating has been undertaken at Scottish Universities Environmental
854 Research Centre. Individual apatite grains were screened based on their clarity and morphology, and hand-
855 picked for (U-Th)/He analysis then packed into Pt tubes prior to analysis. Helium, U and Th analytical
856 protocols adopted in this study follows those described by Foeken et al. (2006, 2007). Length and width
857 measurements for alpha ejection correction (FT; Farley, 2002), were taken for each grain. (U-Th)/He dates
858 were calculated using standard procedures developed by Meesters and Dunai (2002). Total analytical
859 uncertainty, computed as a square root of squares of weighted uncertainties of U, Th and He measurements,
860 and including the estimated additional variation of \pm 7% determined on repeat analyses of Durango apatite.
861 Data are reported in table A4.

862 Appendix captions

863 Table A1 – Selected analyses of mineral phases in monzogranite (RG14) and in a felsic dyke (LCA 7).

864 Table A2 – Selected analyses of accessory phases in monzogranite (RG14) and felsic dyke (LCA 7).

865 Table A3 – LA-ICP-MS isotopic data of zircon from RG12 and RG14 samples.

866 Table A4 – (U+Th)/He data of apatite from RG12 and RG14 samples.

867 Figure captions

868 Fig. 1 - Structural sketch map of Northern Tyrrhenian Basin and Northern Apennines. The main Pliocene–
869 Quaternary basins, transfer zones and Neogene–Quaternary intrusive bodies are indicated (after Dini
870 et al., 2008).

871 Fig. 2 - Geological sketch map of Elba Island. The main faults, the study area and the location of the dated
872 (²⁰⁶Pb/²³⁸U in zircon) samples (RG12 and RG14) are indicated.

873 Fig. 3 – a) Google Earth photograph of the Barbarossa bay where the analyzed monzogranite is exposed;
874 the main structural elements and the mineralized volume corresponding to the Zuccale Fault is also
875 indicated; b) geological sections across the bay with the main structural elements; c) panoramic view
876 of the eastern side of the bay with the main faults and the analyzed monzogranite; d) detail of an
877 extensional detachment fault accompanying the deformation in the footwall of the Zuccale Fault; the
878 stereographic diagram (lower hemisphere, equiareal projection) illustrates the poles of the minor
879 faults linked to the detachments and their kinematics.

880 Fig. 4 – a) Aligned K-feldspar megacrysts defining the magmatic foliation of the monzogranite; b) details of
881
882

883 K-feldspar megacrysts; c) panoramic view of the Capo Bianco promontory with the tectonic relations
884 of the monzogranite and the hosting rocks; d) euhedral corundum growing within quartz-free, biotite-
885 rich domain of the micaschist next to the monzogranite.

886 Fig. 5 - Geological map of the Capo Bianco promontory. Stations of structural analyses and relative data are
887 reported in stereographic diagrams (lower hemisphere, equal-area projection). The location of the
888 analysed samples for microstructural analyses is also indicated. Structural and kinematic data of each
889 fault generation, as described in the text, are reported in stereographic and rose diagrams (lower
890 hemisphere, equal-area projection).

891 Fig. 6 – Bouguer gravity field after Milano et al. (2019). Isolines are in mGal. NE-trending faults are matching
892 the low gravimetric trend, that is here related to a regional transfer zone where magmatic bodies
893 emplaced.

894 Fig. 7 – a) dm-thick felsic dykes intruded within micaschist affected by second generation extensional faults;
895 b) felsic dyke intruded within the monzogranite sampled for microstructural analyses (sample RG2);
896 c) detail of the felsic dyke analysed with EBSD, illustrating the internal foliation and S-C fabric; d) L-
897 tectonite consisting of tourmaline lineation developed on the felsic dyke-surface foliation; e)
898 hydrothermal quartz-rich vein and the mylonitic foliation affecting the adjacent monzogranite.

899 Fig. 8 - Micrographs of petrographic features of the Porto Azzurro monzogranite in plane polarized (PPL)
900 and crossed polars (CP) light. a) Karlsbad twinned K-feldspar with perthitic exsolution lamellae; b)
901 plagioclase with oscillatory zoning (CP image); c) basal section of biotite including elongated apatites
902 and tiny zircon and monazite crystals surrounded by metamictic halos (PPL image); d) K-feldspar-
903 Quartz granophyric intergrowth (CP image).

904 Fig. 9 - Photographs illustrating details of the second generation faults in the Barbarossa bay and Capo
905 Bianco promontory: a) meter-thick tourmaline-rich mineralized fault at the boundary between the
906 monzogranite and the host rocks; b) shear veins parallel to cm-thick fault zones mineralised by quartz
907 and tourmaline, dissecting a dm-thick felsic dyke; c) panoramic view of the low-angle normal faults
908 characterizing the footwall of the Zuccale Fault; d) detail of a fault zone mineralized by tourmaline
909 and quartz characterizing the footwall of the Zuccale Fault and affecting the monzogranite; e)
910 detail of a fault zone mineralized by Fe-oxyhydroxides characterizing the footwall of the Zuccale Fault
911 and affecting the micaschist in the fault system shown in (c).

912 Fig. 10 - Photographs illustrating second generation faults: a-b) panoramic view of the extensional fault
913 system separating the monzogranite from the roof rocks (micaschist) characterizing the footwall of
914 the Zuccale Fault in the Capo Bianco promontory; c) detail of a cm-thick felsic dykelet assisting
915 deformation along the slip surface of the fault zone illustrated in (a) and (b); d) felsic dykelet injected
916 in the cataclasite and ductilely deformed during faulting.

917 Fig. 11) - Photographs illustrating details of the third generation faults affecting the monzogranite in the
918 Capo Bianco promontory: a-b) horsetail fractures developed in the tip-damage zone of a right-lateral
919 strike-slip fault; c) dm-sized extensional jog formed in the linking damage zone of two overstepping
920 right-lateral strike-slip faults; d-e) detail of a right-lateral strike-slip fault zone and minor (i.e. splay)
921 structures.

922 Fig. 12 – EBSD misorientation maps of sample RG2. a) Kfs shown with IPF color coding, quartz distinguished
923 as phase (red) and plagioclase shown in band contrast mode (grey tones). Boudinaged Kfs
924 recrystallizes to new grains in the neck, showing crystallographic mismatches between 10 and $> 90^\circ$;
925 b) anastomosing recrystallized quartz bands (IPF color coded) show a large preference for reddish
926 colors, proving that the c-axis distribution of recrystallized grains is oriented towards the observer.
927 Maximum of crystallographic mismatches along grain boundaries is $> 30^\circ$.

928 Fig. 13 - Pole figures, equal area projections, lower hemisphere. a) Multiples of Mean Unit Densities
929 expressed by color bars. Bar with maxima just above 7 belong to pole figures b,c,e, while bar with
930 maximum at 14 belongs to pole figure d; b) pole figure of recrystallized grains in the neck of the
931 boudinaged Kfs (Fig. 12a). White line is foliation trace. Maximum of $\{110\}$ poles is consistent with this
932 plane being the slip plane, while dispersion of slip direction $\langle 1-12 \rangle$ in a girdle centered on that
933 maximum suggests that dislocation creep was accommodated by grain boundary sliding; c) quartz c-
934 axis of grains within anastomosing bands within sample RG2 form a maximum in the central part of
935 the pole figure, while poles to a- and m-prisms are dispersed along the equatorial section of the pole
936 figure; d) distribution of c-axes within recrystallized quartz-rich band in sample RG2 forms a

937 pronounced maximum in the center, while poles to a- and m-prisms form single maxima consistent
938 with dextral shear and activation of prism $\langle a \rangle$ slip; e) quartz c-axis distribution within recrystallized
939 grains of mylonitic monzogranite (sample RG₄, Fig. 15b) forms a typical type-I crossed girdle,
940 suggesting activation of basal $\langle a \rangle$, rhomb $\langle a \rangle$ and prism $\langle a \rangle$ slip, and hence lower deformation T than
941 for sample RG₂.

942 Fig. 14 - Micrograph of a discrete shear zone localized within Sample RG₄ and EBSD analysis areas. a) The
943 foliated monzogranite (top) evolves to a mylonite in correspondence of EBSD analysis area Fig. 15a.
944 There is a deformation gradient from mylonite towards ultramylonite next to the quartz-rich vein with
945 green tourmaline clasts; b) sketch of Fig. 14a highlighting the different deformational domains: G =
946 foliated monzogranite; GM = mylonite ; UM = ultramylonite. Location of Figures 15a and b is also
947 shown.

948 Fig. 15. EBSD misorientation maps (IPF color coding) of the areas indicated in Fig. 14. a) Monzogranite next
949 to the mylonite boundary. Large quartz crystals are still preserved showing evidence of sub-grain
950 boundaries. Recrystallization starts at sites of stress localization. Crystallographic mismatches are
951 between 10 and $>60^\circ$. The small grain size and evidence for mixing up of recrystallized grains
952 belonging to different quartz domains suggest grain-boundary sliding to have been important; b)
953 monzogranite deformed at higher strain. Quartz is fully recrystallized and forms a mylonitic foliation
954 trending ENE-WSW in the map. Some remnants of larger grains with core and mantle structure are
955 still preserved. Maximum misorientation of adjacent grains is larger than 30° . Variegated colors of
956 grains testify that slip occurred along multiple systems during mylonitic deformation. Non indexed
957 grey phases are Kfs and plagioclase.

958 Fig. 16 – Selected BSE-CL images of zircon grains from samples RG₁₄ (a-d) and RG₁₂ (e-h) representative
959 of different CL features. Location of LA-ICP-MS spots is shown as well as Zrc#. Scale bar is 50 μm .

960 Fig. 17 – $^{206}\text{Pb}/^{238}\text{U}$ zircon data for RG₁₄ and RG₁₂ samples. U-Pb data are ordered and shown as vertical bars
961 comprising 2sigma errors. Grey filled bars were considered for calculation of weighted average ages
962 (horizontal hemi transparent boxes). Available U-Pb zircon data, with relative errors, for the Porto
963 Azzurro pluton are also shown: white circles refer to SIMS U/Pb ages from three zircon grains in
964 Gagnevin et al. (2011); black square is the LA-ICP-MS U/Pb age of a zircon rim from the contact
965 aureole (Musumeci et al., 2011).

966 Fig. 18 - T-t diagram showing the cooling history of the Porto Azzurro monzogranitic pluton reproduced for
967 1 Myr after the magma emplacement fixed at 6.4 Ma at a depth of c. 6.5 km. The two cooling curves
968 result from a static model (black line) and a dynamic model (grey line), incorporating the effect of
969 unroofing simulated by an exponential law (see Table 1). Details of the modelling are provided in
970 Caggianelli et al. (2018) and Caggianelli et al. (2014). Age obtained from zircon is plotted at the
971 corresponding saturation temperature. Age of biotite (Maineri et al., 2003) is plotted at the
972 corresponding closure temperature, calculated by Dobson (1973) formula.

973 Fig. 19 - Depth - strength diagrams at 300 kyr, 600 kyr and 1 Myr. They show depth of the brittle/ductile
974 transitions and the contact between the Porto Azzurro monzogranite with the roof rocks. (a) Static
975 model; (b) dynamic model incorporating the effect of unroofing.

976 Fig. 20 - z-t diagram showing the depth change of the rheological boundaries (black and blue lines) and of
977 the monzogranite - roof rocks lithological boundary (grey line), as reproduced by a static (a) and
978 dynamic model (b). The simulation lasts 1 Myr starting from 6.4 Ma and from a magma emplacement
979 depth of 6.5 km. The shallower brittle-ductile (B/D) transition (black line), within the roof rocks,
980 culminates to a minimum depth in correspondence of point x and disappears after point y. The deeper
981 B/D transition (blue line), within the monzogranite, starts from point z and progressively sinks. The
982 co-existence of B/D transitions is confined to the time interval between z and y points. The rheological
983 evolution of the top of the pluton, relevant for the Capo Bianco outcrop, can be followed along the
984 grey line. Thus, the points z and y mark the transition to the brittle domain for the monzogranite and
985 the roof rocks, respectively.

986
987 Table 1 - Physical parameters used in the thermal model.

988
989 Table 2 - Flow law constants adopted for the dislocation creep exponential equation.

990

991
992

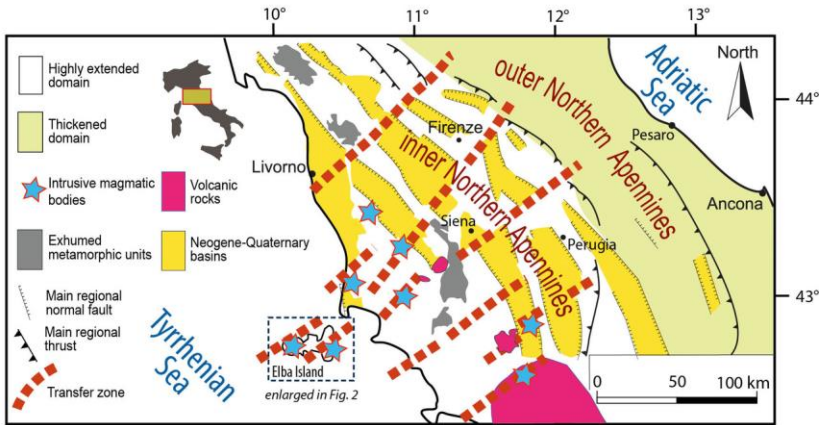


Fig.1

993
994
995

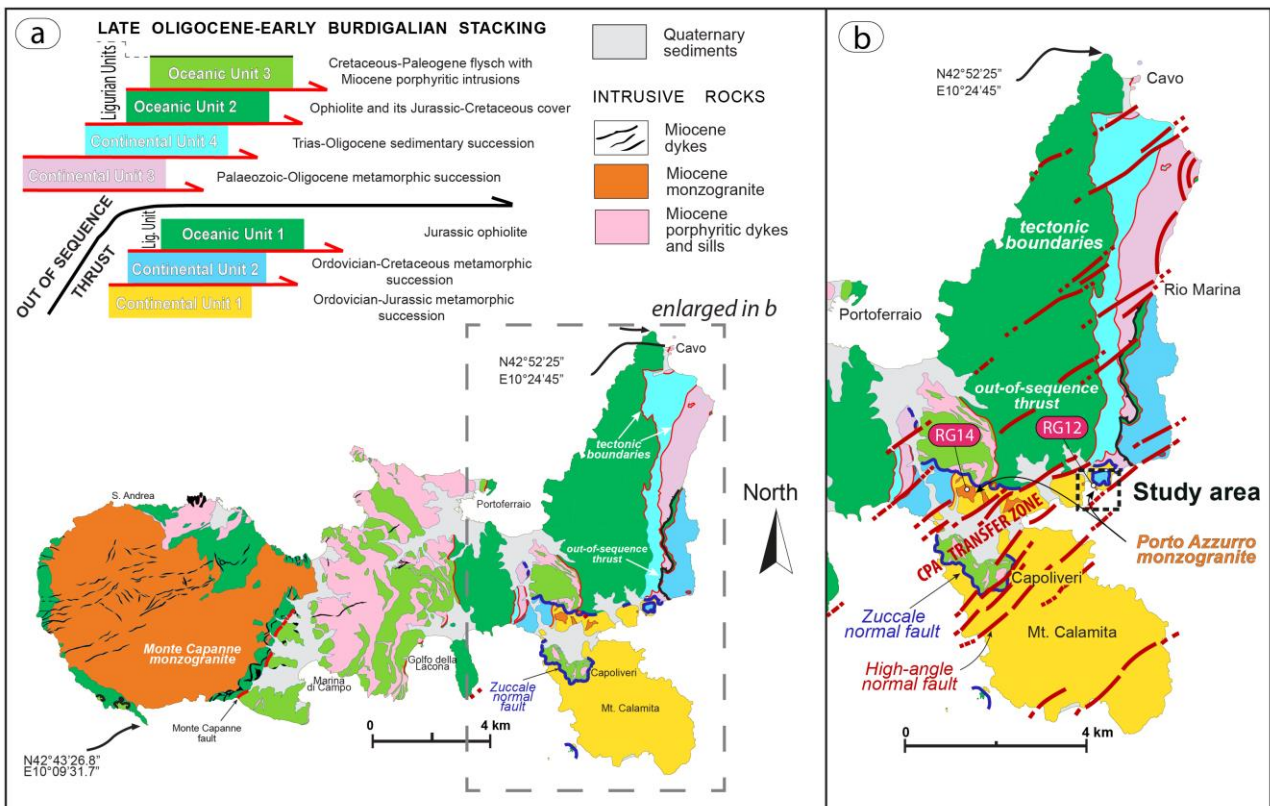
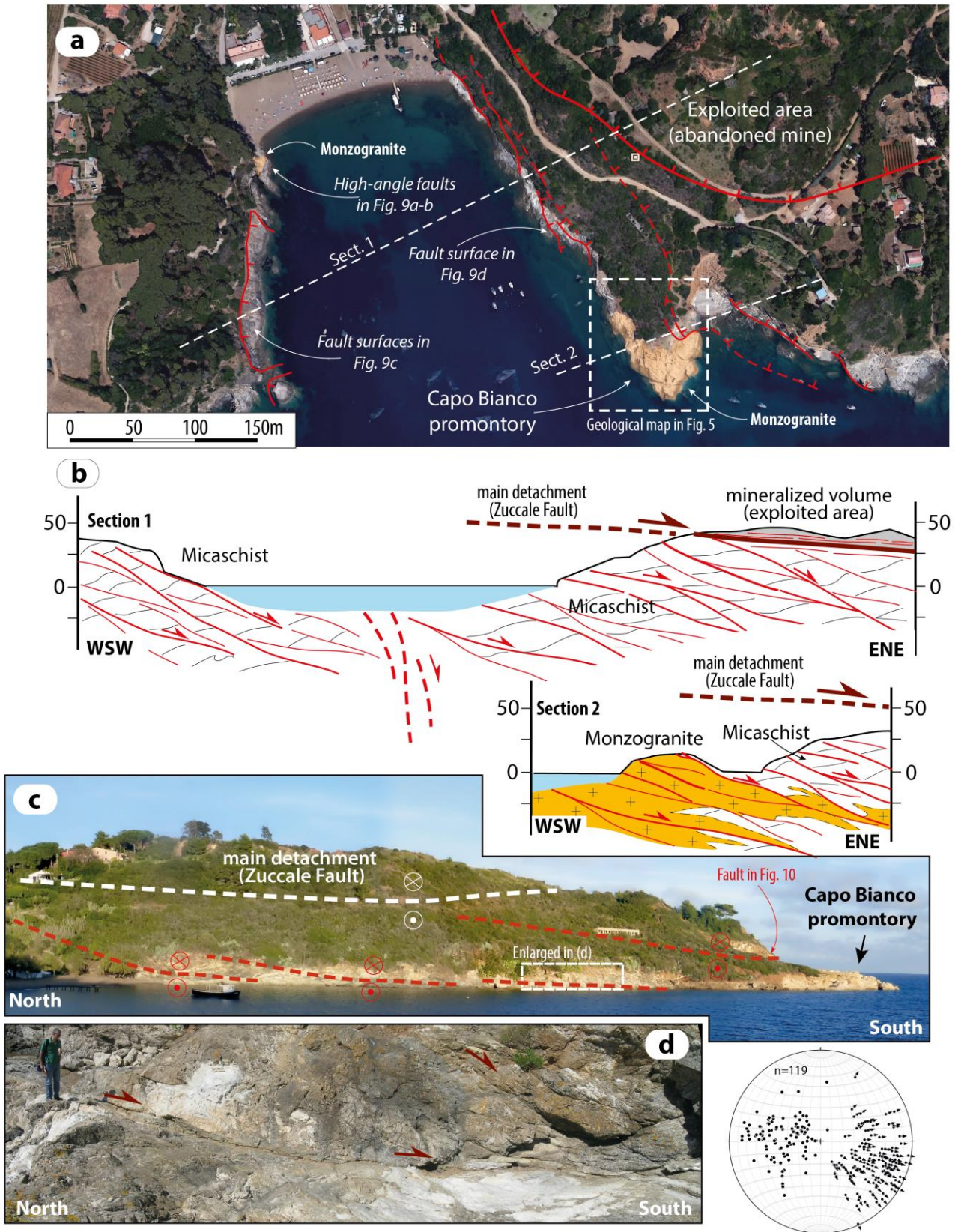
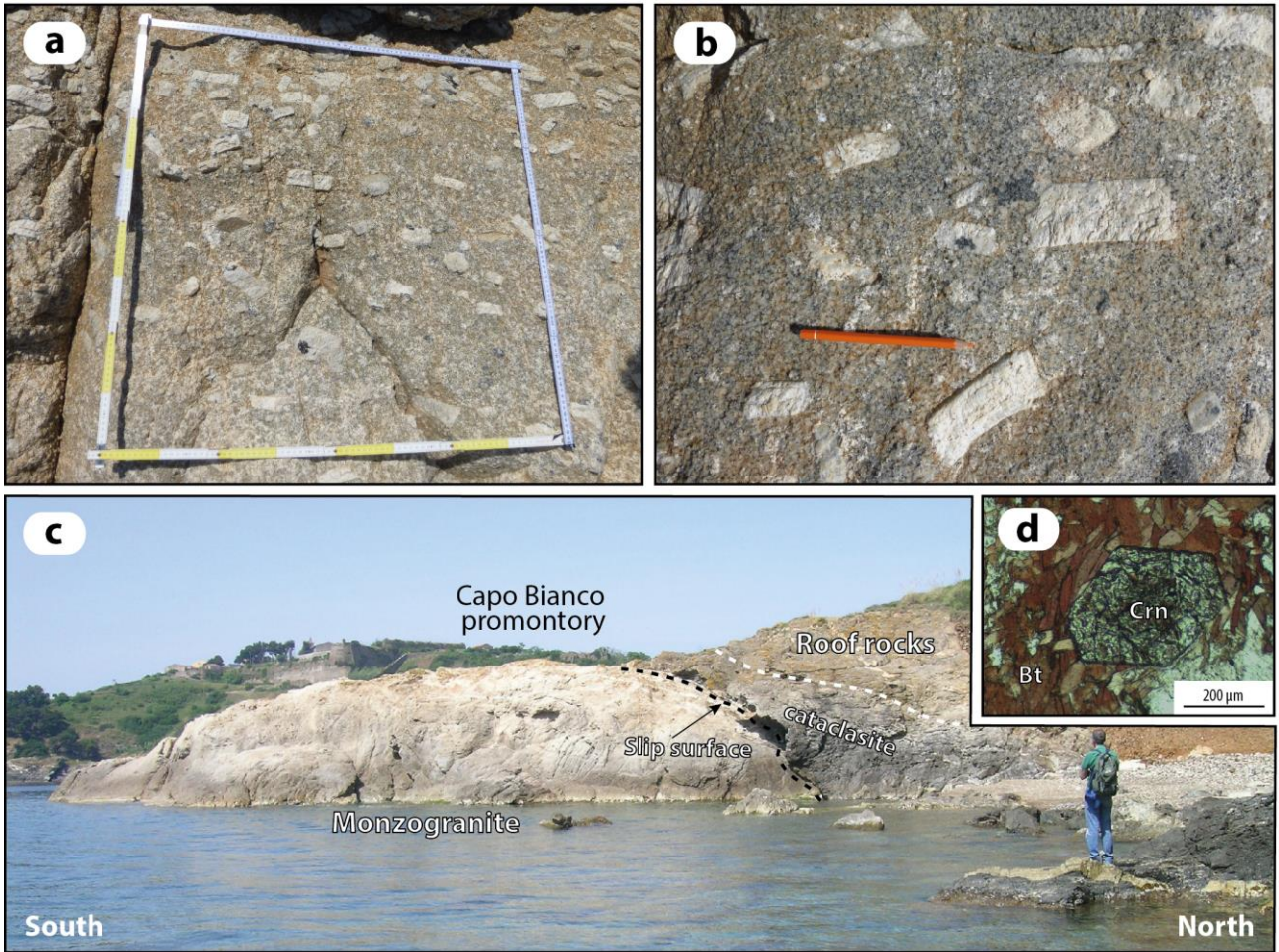


Fig. 2

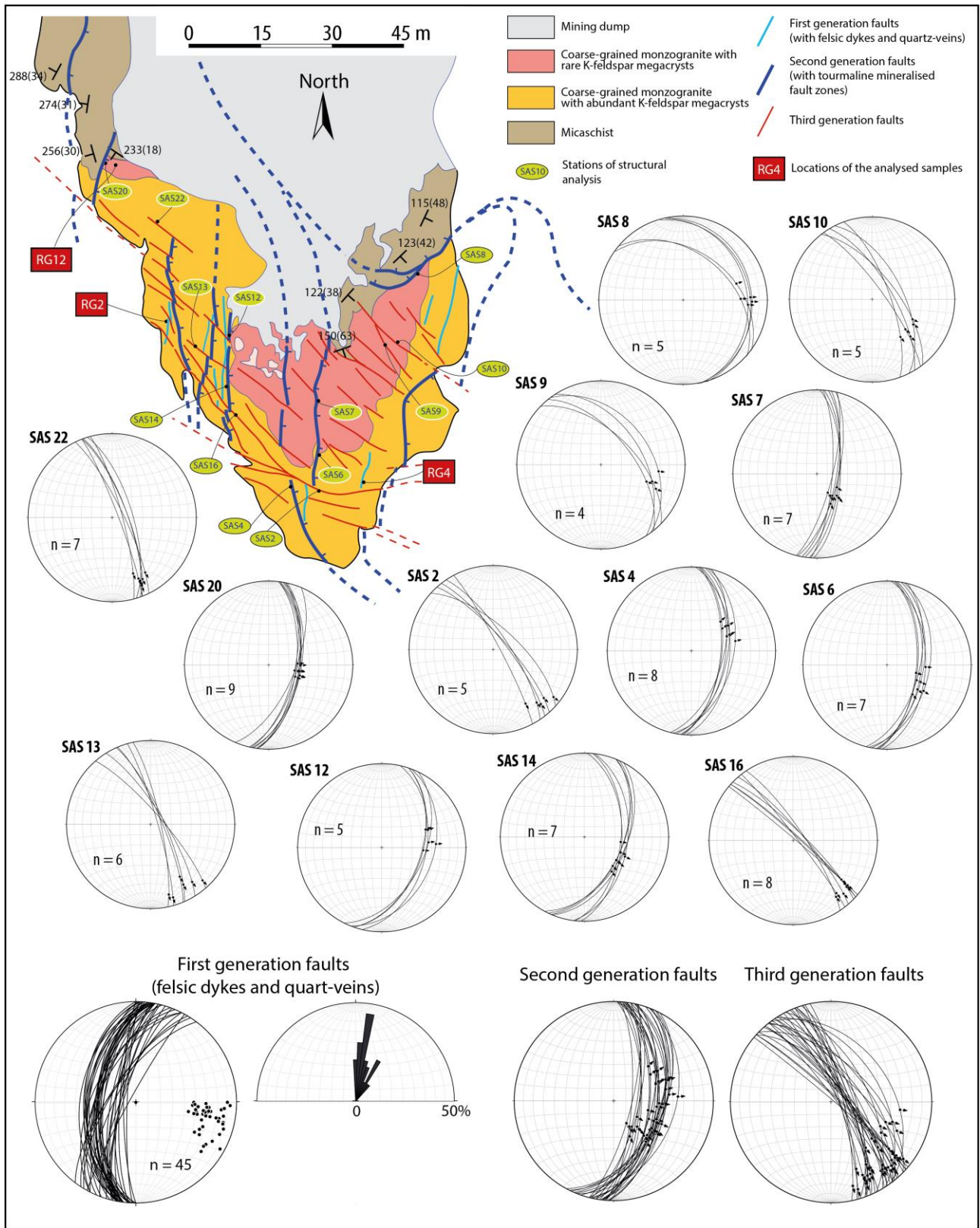
996
997
998



999
 1000 Fig. 3
 1001



1002
1003 Fig.4



1004
1005

Fig.5

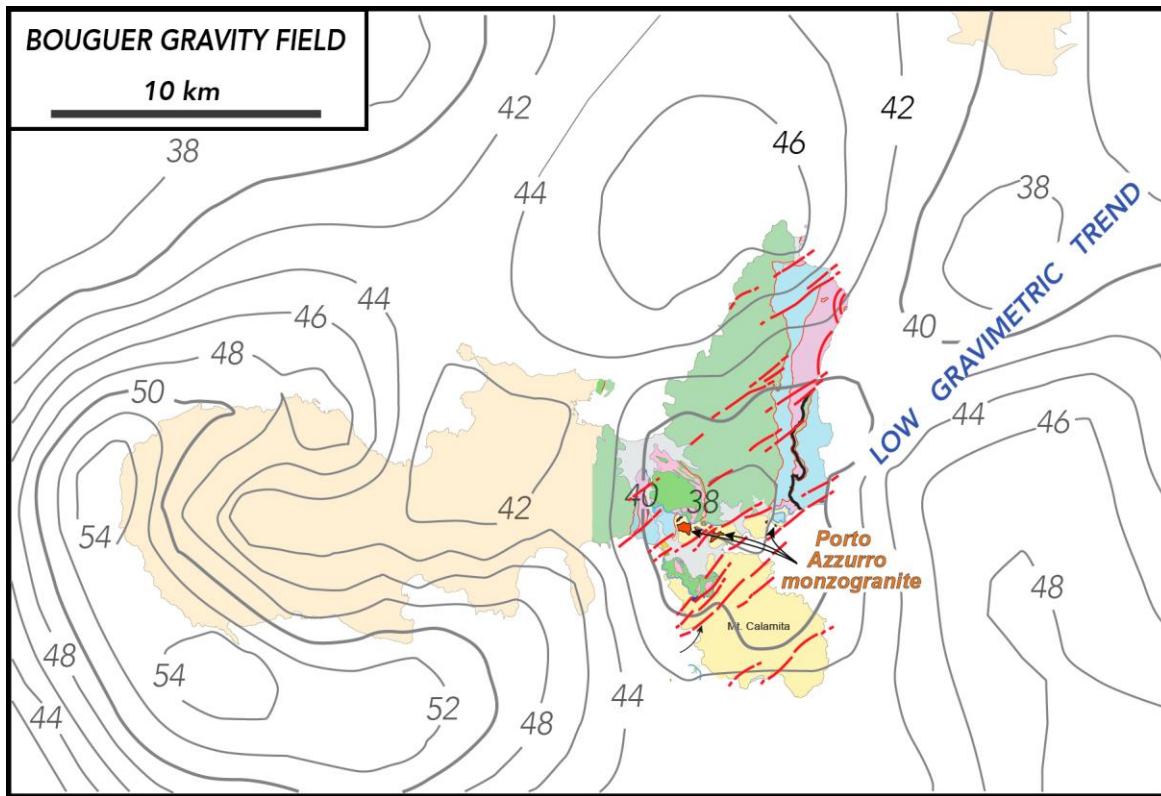
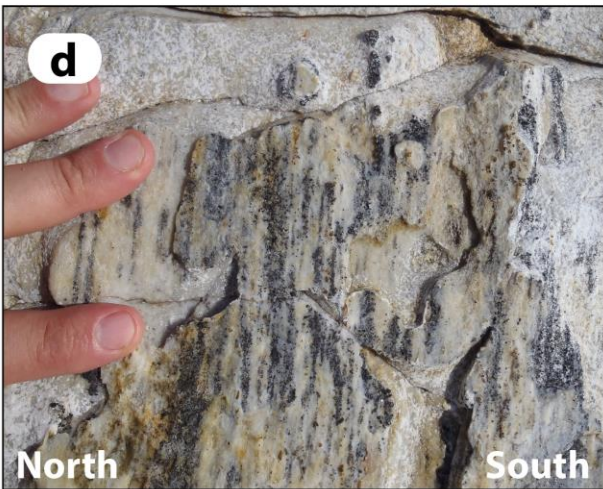
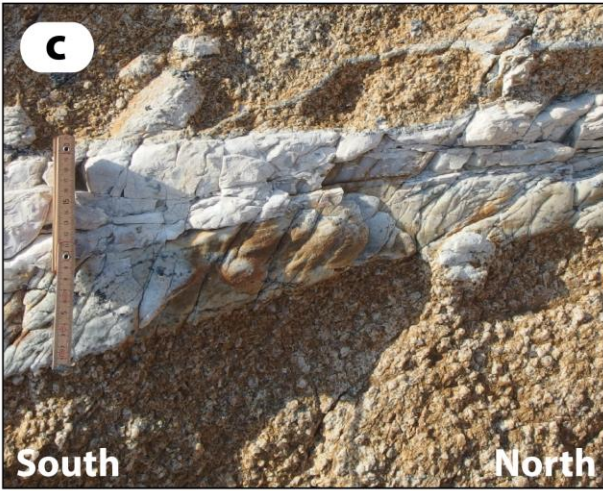
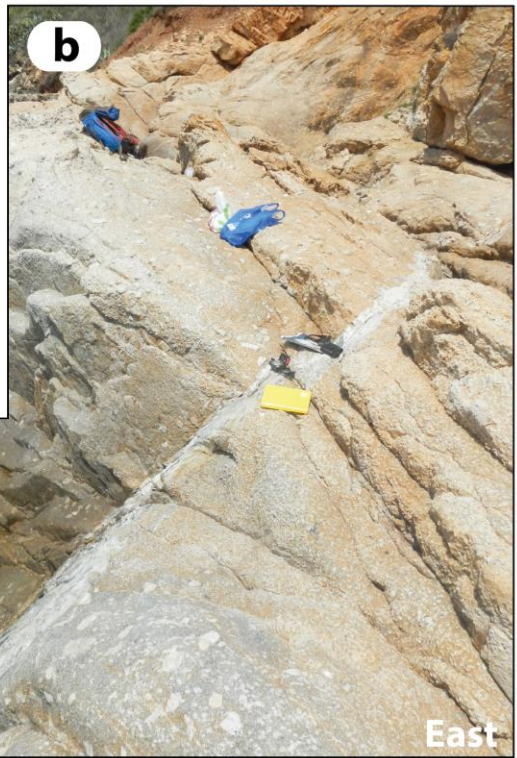


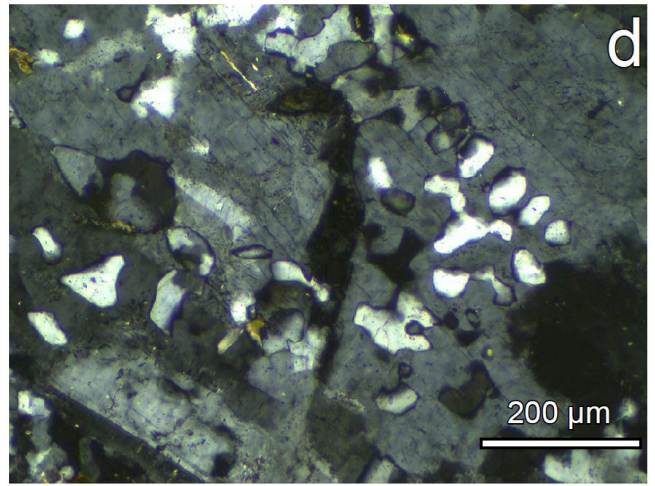
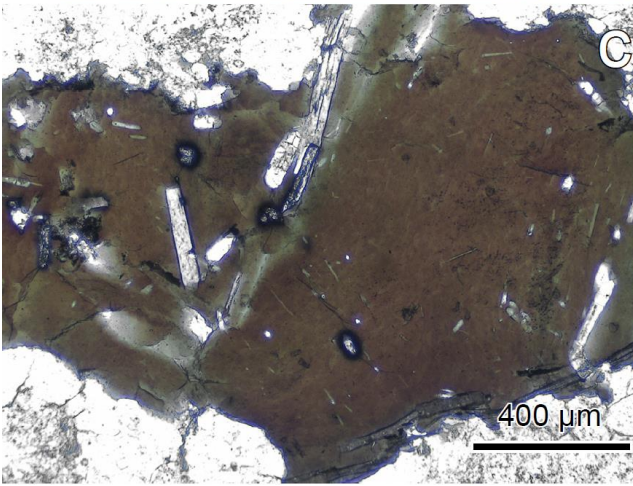
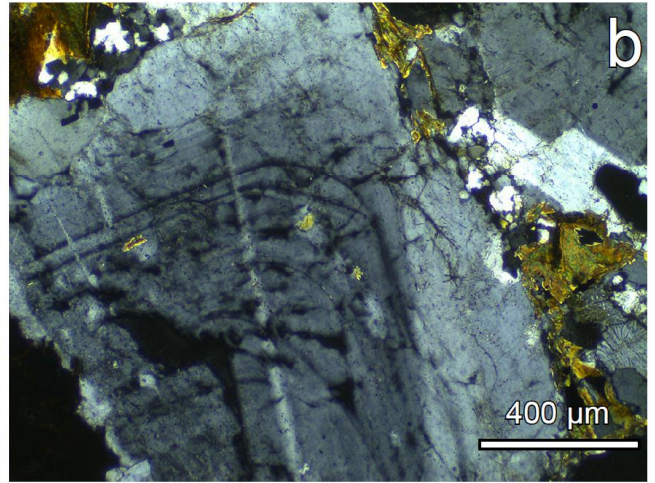
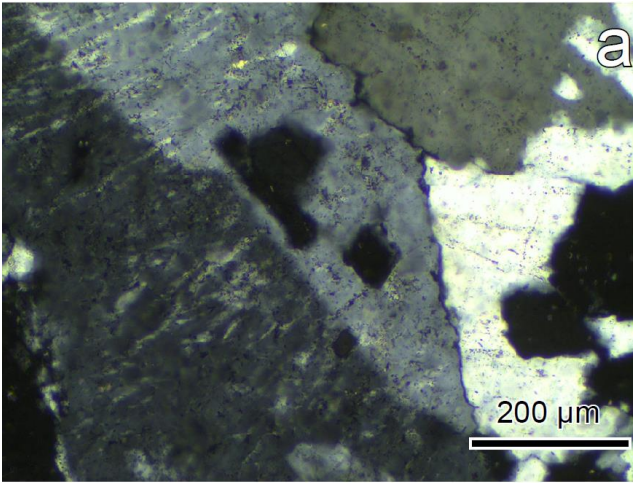
Fig.6

1006
1007
1008



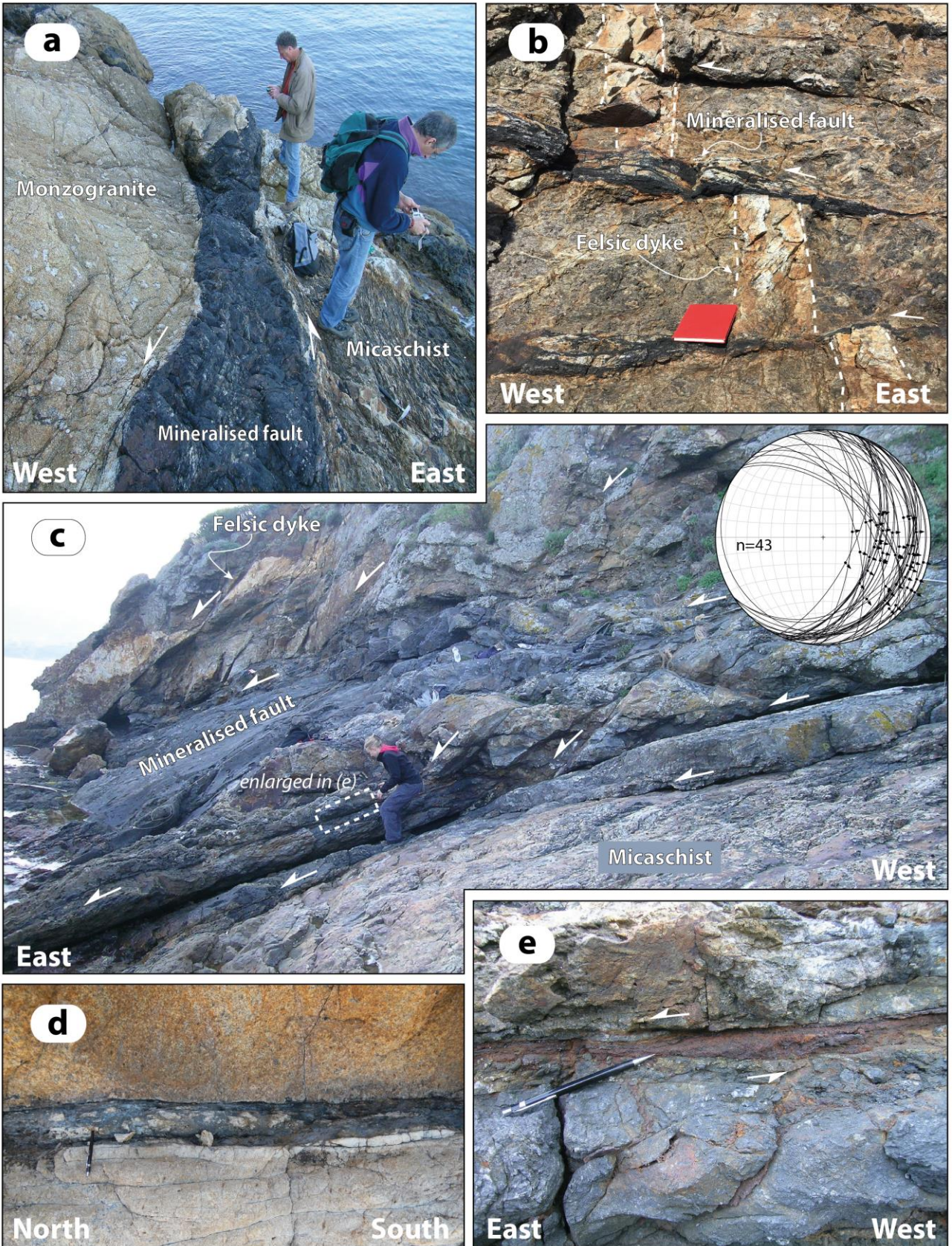
1009
1010
1011

Fig.7



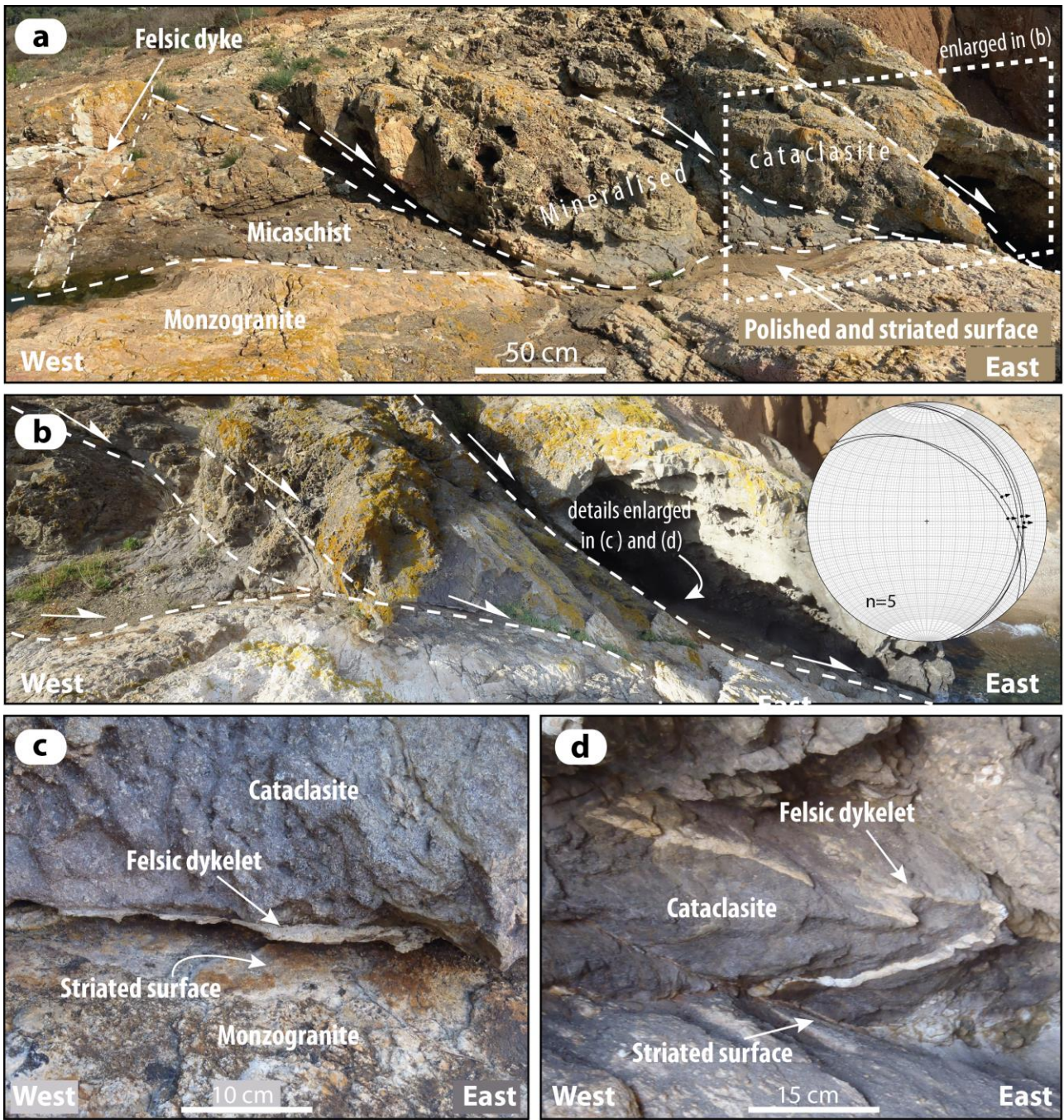
1012
1013
1014

Fig.8

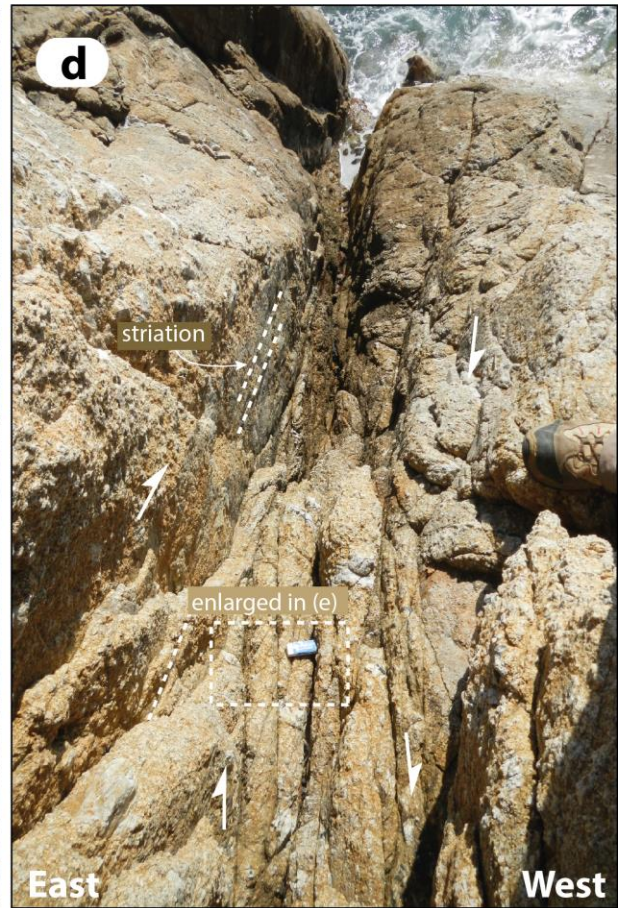
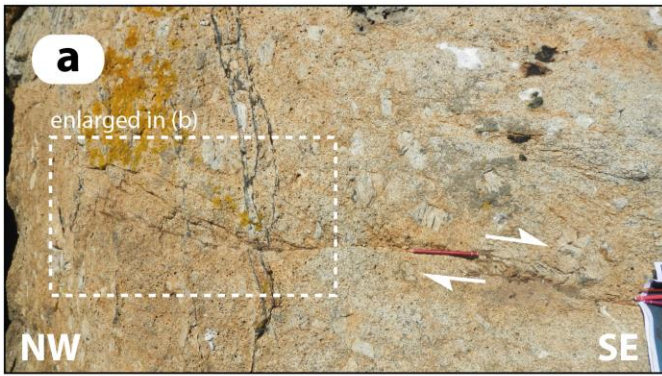


1015
 1016
 1017

Fig. 9

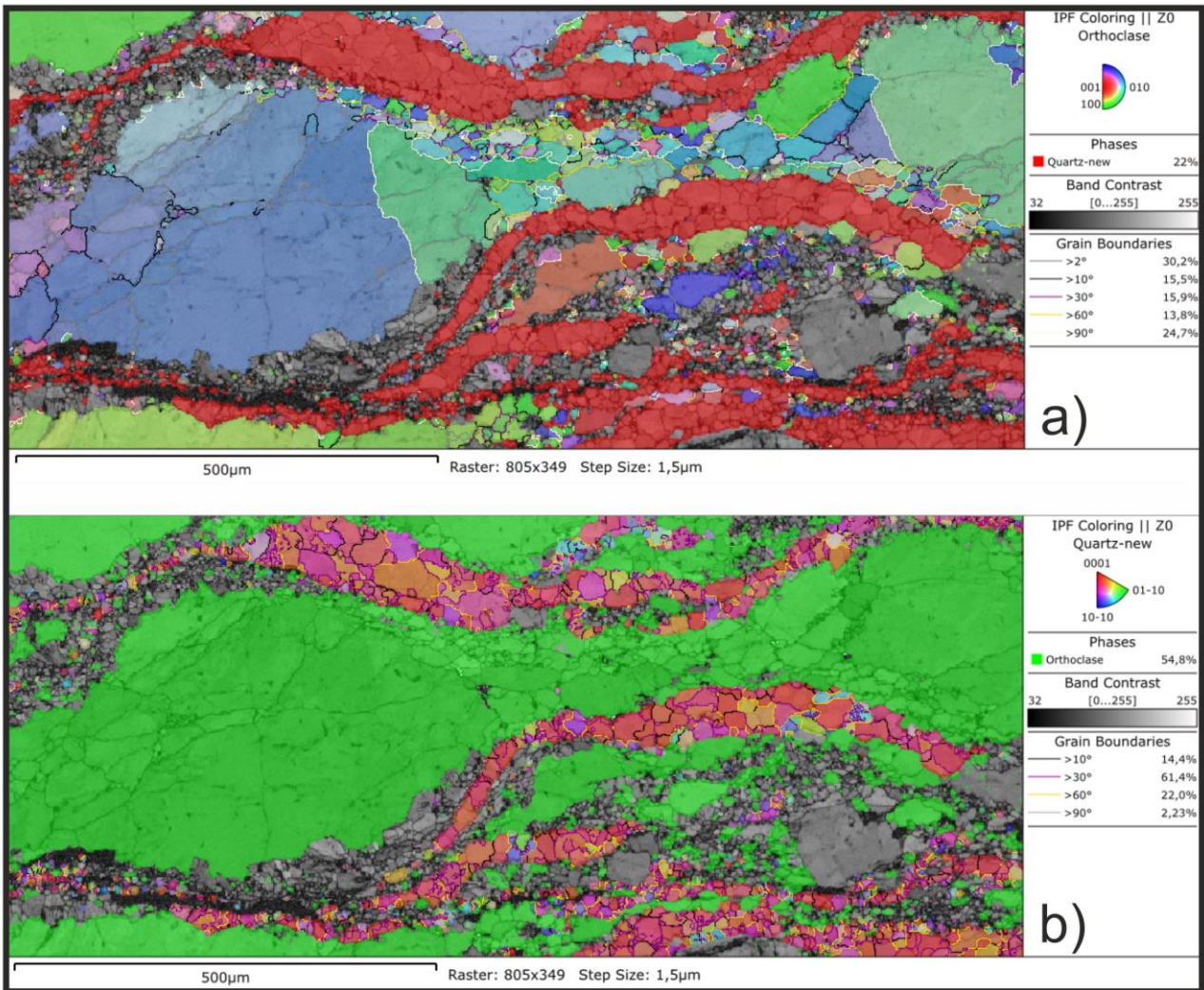


1018
1019
1020
Fig. 10



1021
1022

Fig.11



1023
1024
1025

Fig. 12

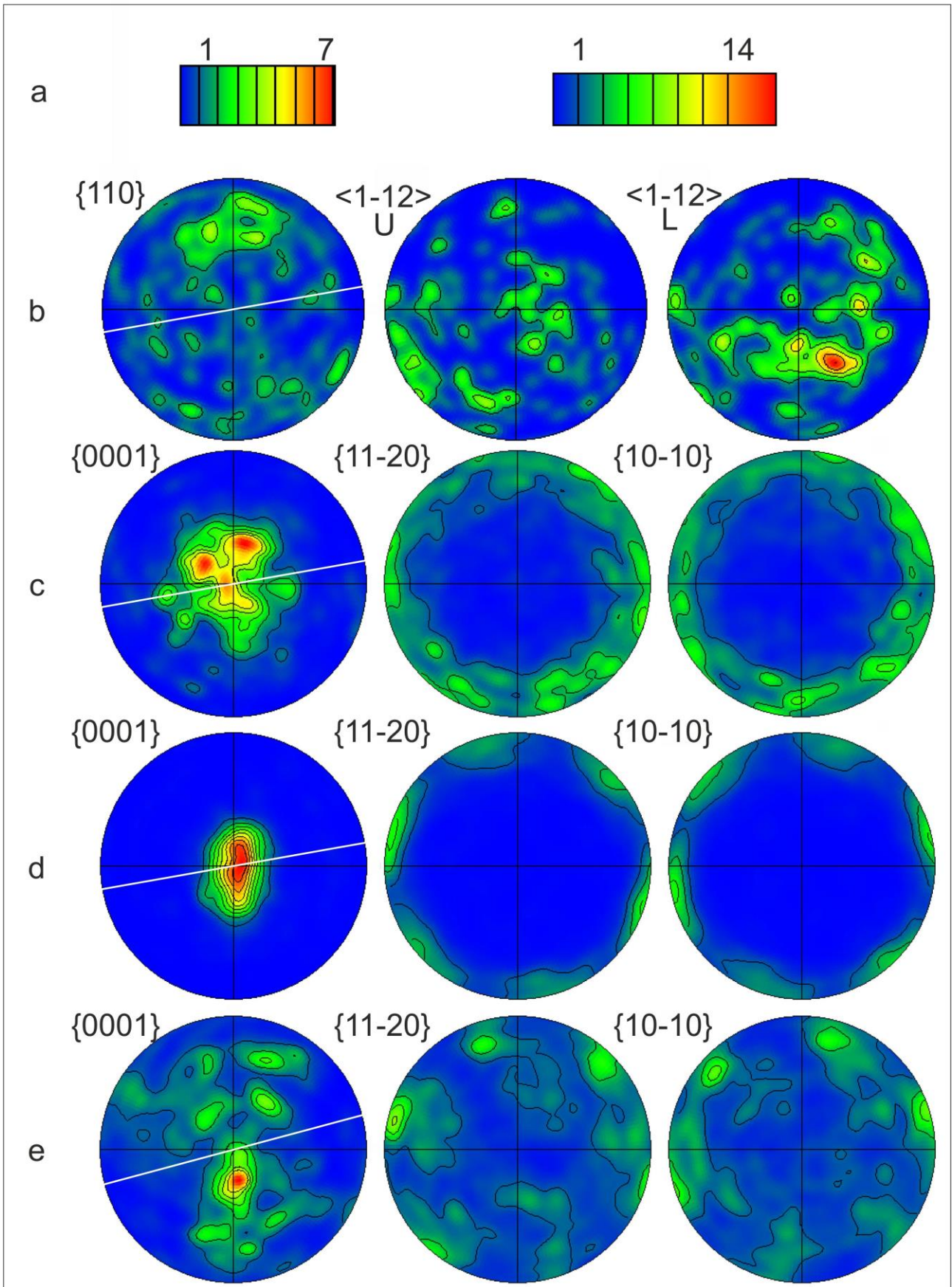
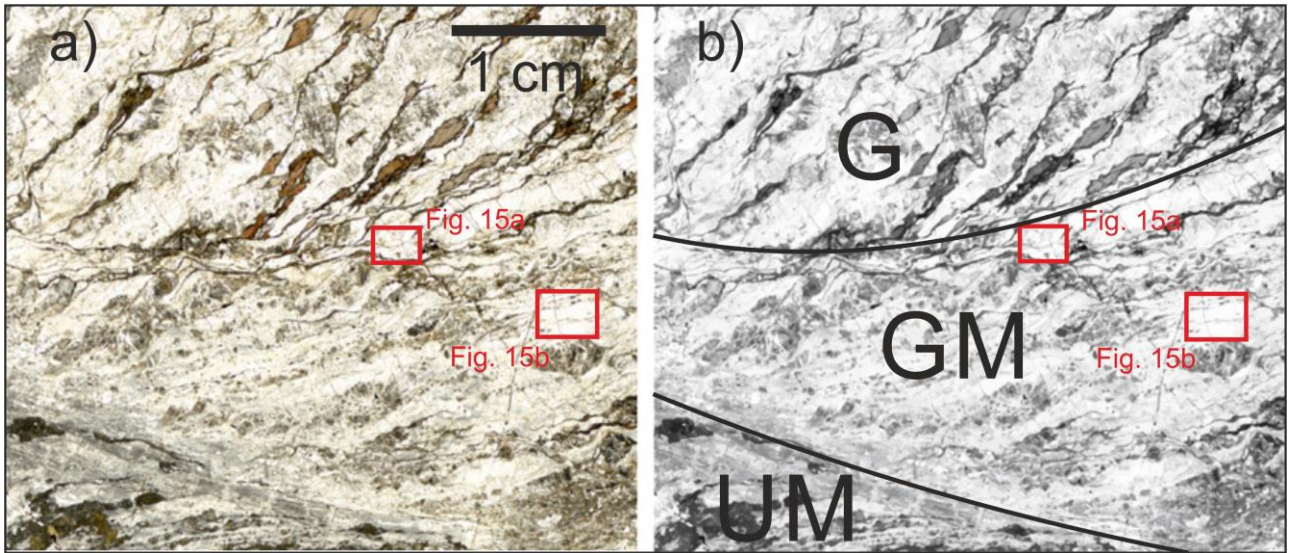


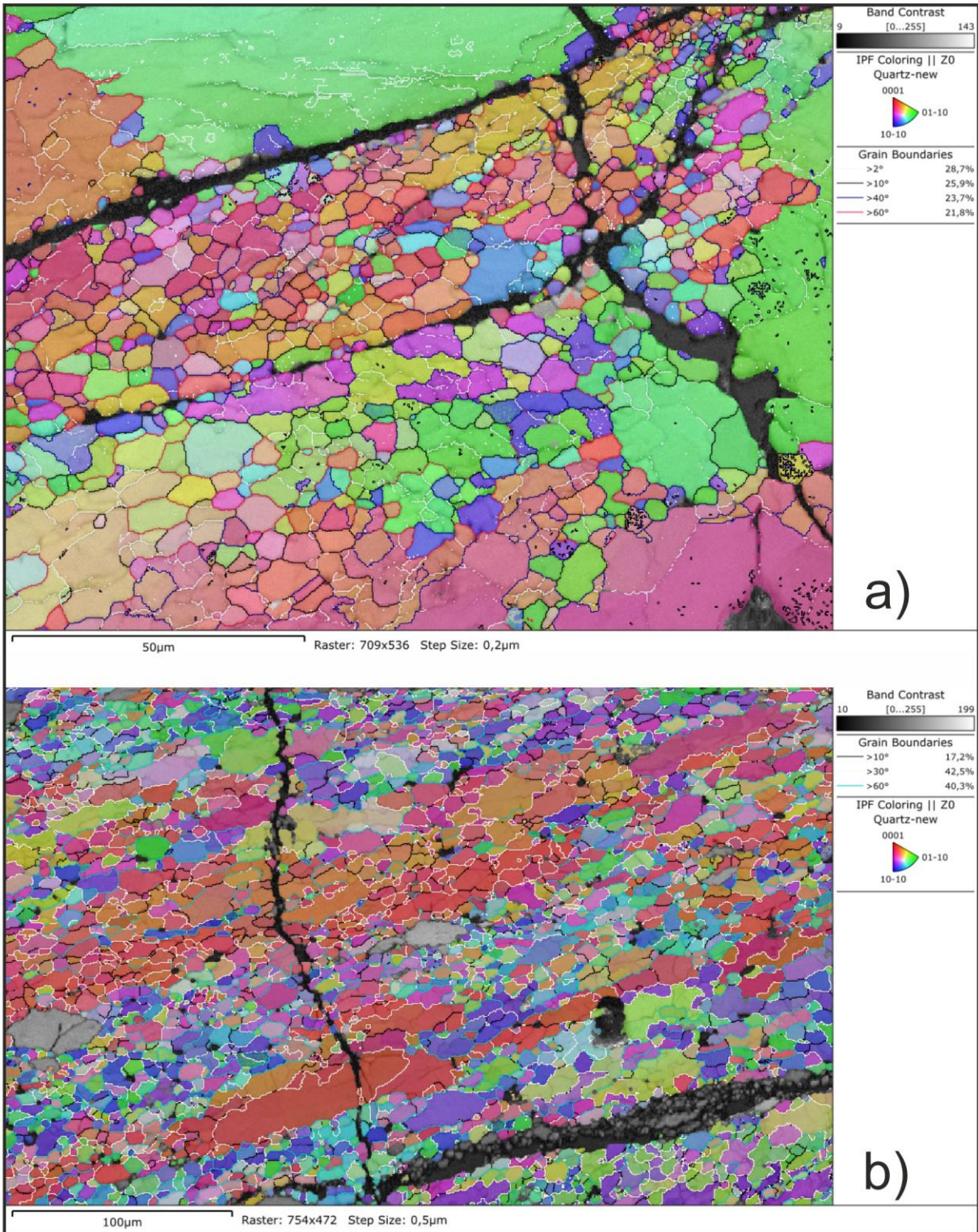
Fig. 13

1026
1027
1028
1029



1030
1031
1032

Fig.14



1033
1034
1035

Fig. 15

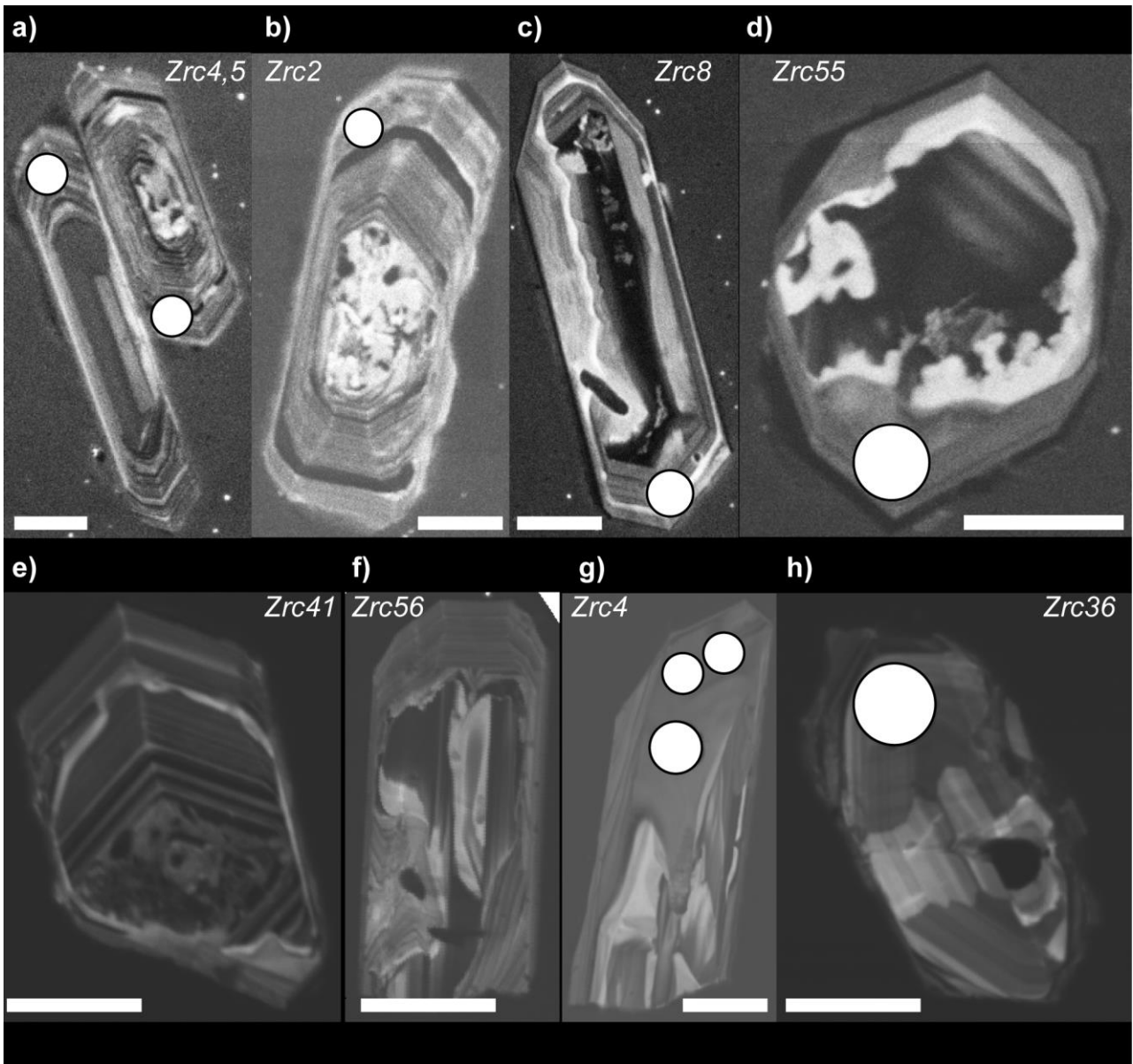


Fig. 16

1036
1037
1038
1039

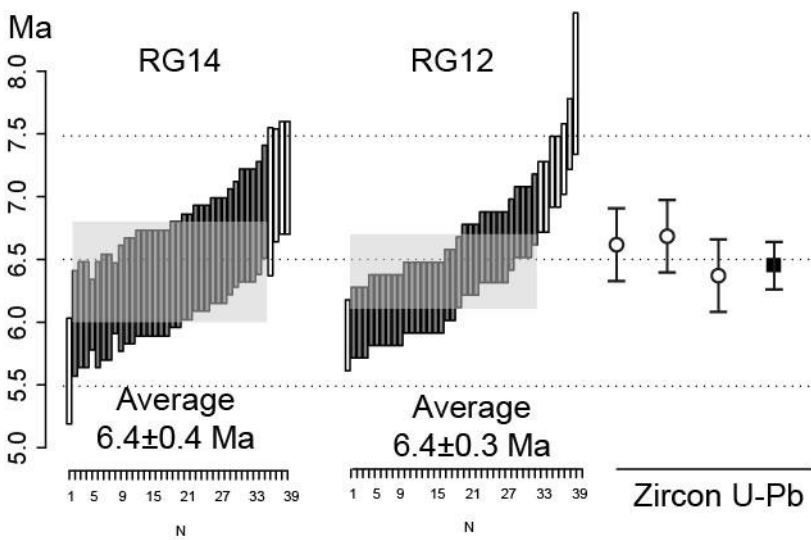
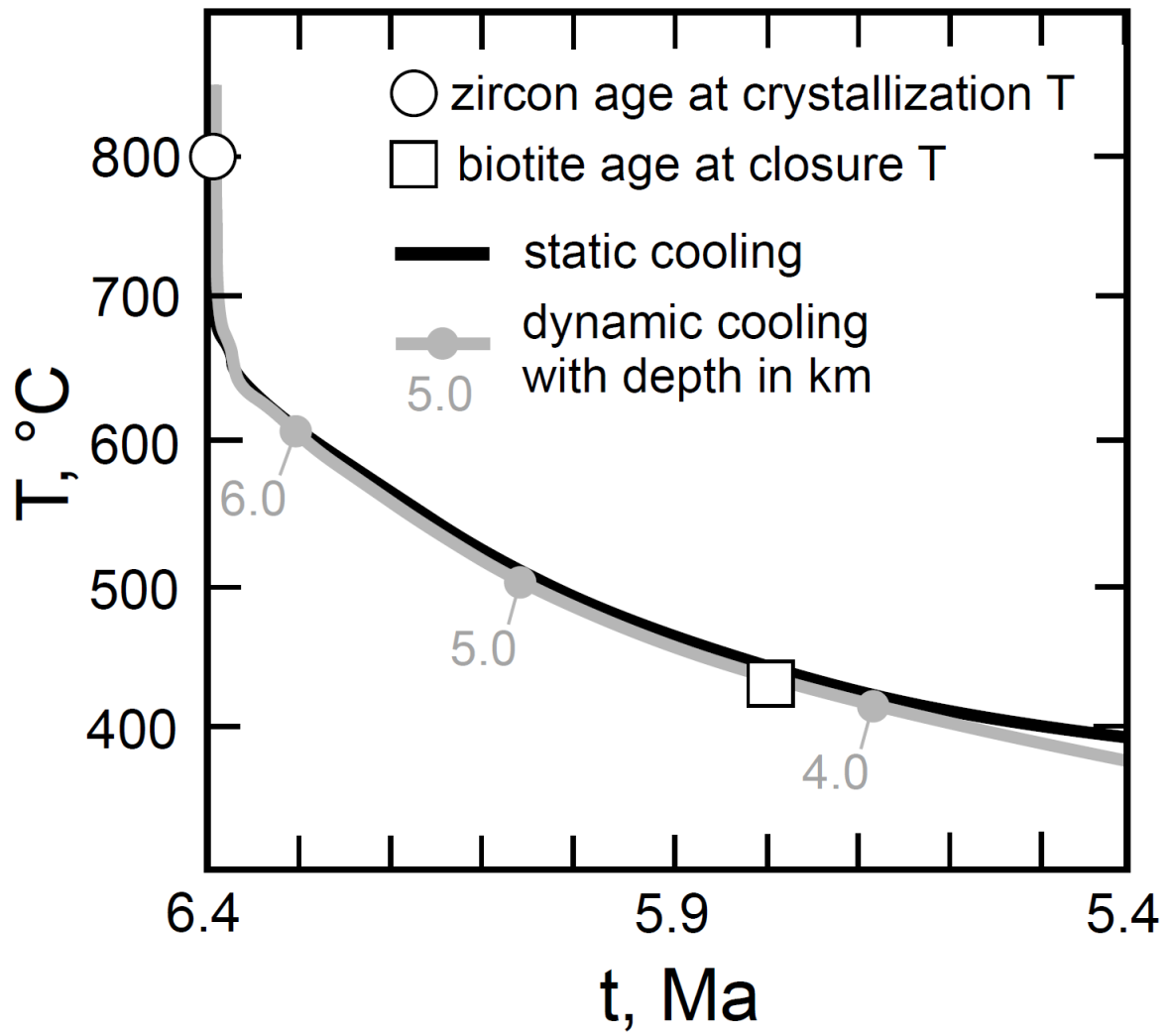
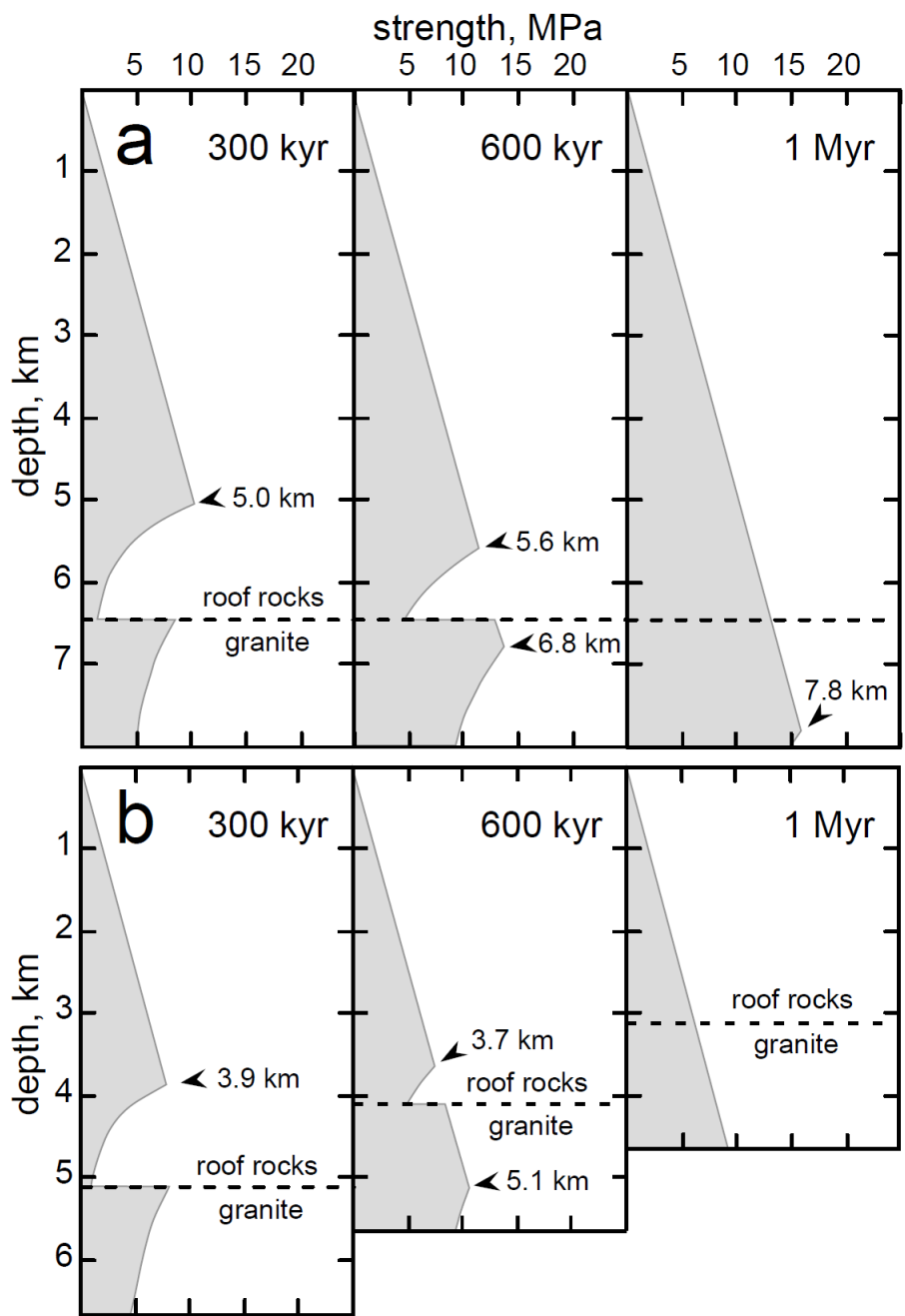


Fig. 17

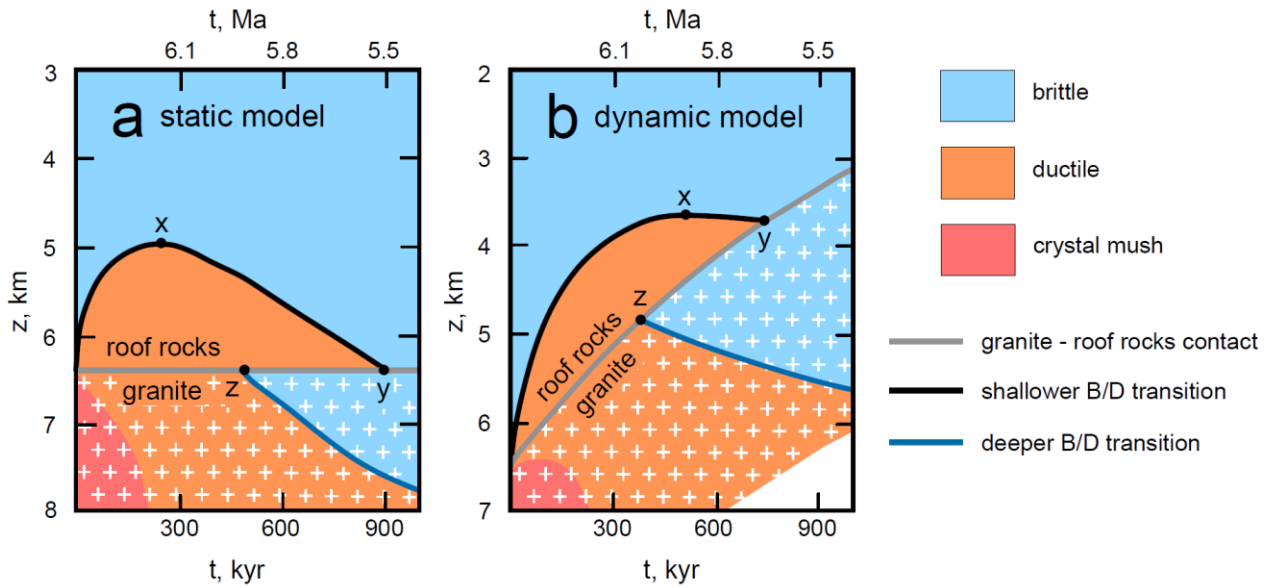
1040
1041
1042



1043
 1044 Fig. 18
 1045



1046
1047 Fig.19
1048



1049
1050
1051
Fig.20

Parameter	Symbols and equations	Values
Thermal conductivity [W m ⁻¹ K ⁻¹]	K	1.85 (crust) 3.35 (mantle)
Density [kg m ⁻³]	ρ	2750 (crust) 3300 (mantle)
Specific heat [J kg ⁻¹ K ⁻¹]	C_P	1000 (crust) 1100 (mantle)
Heat generation rate [μ W m ⁻³]	$A = A_0 e^{(-z/D)}$	$A_0 = 2$ $D = 12000$ m
Latent heat of crystallization [kJ kg ⁻¹]	ΔH	300 (for a T range of 850-650 °C)
Unroofing rate [m yr ⁻¹]	$v_z = dz/dt = -c z$	$v_z (t=0) = 5 \times 10^{-3}$ m yr ⁻¹ $c = 8.93 \times 10^{-7}$ yr ⁻¹

1052
1053
1054
Table1

	Lithology	Rheological analog	Creep parameters		
			A_c [MPa ⁻ⁿ s ⁻¹]	n	E [J mol ⁻¹]
Roof rock	micaschist and quartzite	wet quartzite	3.2×10^{-4}	2.3	1.54×10^5
Pluton	monzogranite	granite	1.80×10^{-9}	3.2	1.23×10^5

1055
1056
1057
Table 2

Table A1 – Selected analyses of mineral phases in monzogranite (RG 14) and in a felsic dyke (LCA 7).

	RG 14							LCA 7						
	Pl core	Pl core	Pl rim	Kfs	Ab	Bt	Bt	Pl core	Pl rim	Kfs	Bt	Bt	Tur core	Tur rim
SiO ₂	59.13	59.18	65.37	65.40	68.41	35.73	36.79	65.18	65.83	64.11	33.57	34.62	35.76	35.49
TiO ₂						4.18	3.97				3.66	3.11	0.47	0.86
Al ₂ O ₃	26.48	25.38	21.68	18.48	19.64	16.90	16.20	21.70	21.79	18.40	17.81	18.97	34.45	34.23
FeO						19.73	19.33			0.23	24.83	23.63	9.46	10.05
MnO											0.37	0.38		
MgO						8.47	9.04				4.55	4.73	3.14	3.16
CaO	8.30	7.49	3.06		0.44			2.78	2.79	0.17			0.20	0.48
Na ₂ O	6.97	7.23	9.75	1.20	10.97	0.33	0.31	9.78	9.58	1.38		0.18	1.54	1.70
K ₂ O	0.15	0.36	0.27	15.56	0.30	9.63	9.59	0.39	0.24	15.15	9.78	9.80	0.09	
B ₂ O ₃ *													10.47	10.51
Li ₂ O**													0.25	0.27
Tot.	101.03	99.64	101.13	100.64	99.76	94.97	95.23	99.83	100.24	99.44	94.58	95.41	95.83	96.75
ΣO	8	8	8	8	8	11	11	8	8	8	11	11	29eLi	29eLi
Si	2.615	2.652	2.873	2.997	2.993	2.744	2.805	2.873	2.883	2.979	2.671	2.700	5.938	5.868
Ti						0.241	0.227				0.219	0.182	0.059	0.107
Al ^{IV}	1.282	1.342	1.124	0.999	1.014	1.256	1.195	1.129	1.126	1.009	1.672	1.746	0.062	0.132
Al ^{VI}						0.275	0.262						6.687	6.546
Fe						1.267	1.233			0.009	1.652	1.541	1.313	1.389
Mn											0.025	0.025		
Mg						0.97	1.027				0.540	0.550	0.777	0.779
Ca	0.393	0.360	0.144		0.021			0.131	0.131	0.008			0.036	0.085
Na	0.598	0.628	0.831	0.107	0.930	0.049	0.046	0.836	0.814	0.124		0.027	0.496	0.561
K	0.008	0.021	0.015	0.909	0.017	0.943	0.932	0.022	0.013	0.898	0.992	0.975	0.019	
B													3.000	3.000
Li													0.164	0.179
Σcat	4.997	5.002	4.988	5.012	4.974			4.991	4.967	5.028	7.770	7.746	18.550	18.550
X _{Fe}						0.566	0.546				0.754	0.737	0.628	0.641

* B₂O₃ calculated assuming 3 B atoms per formula units. ** Li₂O calculated by charge balance.

1058
1059

Table A2 – Selected analyses of accessory phases in manozogranite (RG 14) and felsic dyke (LCA 7).

	RG 14				LCA 7	
	Zrc	Mnz	Mnz	Ap	Zrc	Mnz
SiO ₂	31.35	2.25	1.23	0.19	29.65	0.60
FeO	0.34			0.82		
MnO				0.67		
CaO		0.54	0.69	55.11		1.55
Na ₂ O				0.12		
P ₂ O ₅		26.50	28.05	43.13		29.19
La ₂ O ₃		16.28	15.54			13.85
Ce ₂ O ₃		30.00	31.00			28.42
Pr ₂ O ₃		2.37	3.19			2.80
Nd ₂ O ₃		10.10	11.32			11.63
Sm ₂ O ₃			1.38			2.37
Gd ₂ O ₃						1.74
ThO ₂	0.97	11.42	8.11			7.14
UO ₂	1.26				5.68	0.74
Sc ₂ O ₃					0.54	
ZrO ₂	65.04				61.00	
HfO ₂	0.34				1.50	
Tot.	99.30	99.46	100.51	101.04	98.38	100.02
ΣO	4	4	4	25	4	4
Si	0.982	0.091	0.049	0.031	0.955	0.024
Fe	0.009			0.113		
Mn				0.093		
Ca		0.023	0.029	9.706		0.065
Na				0.038		
P		0.911	0.946	6.002		0.974
La		0.244	0.228			0.201
Ce		0.446	0.452			0.410
Pr		0.035	0.046			0.040
Nd		0.146	0.161			0.164
Sm			0.019			0.032
Gd						0.023
Th	0.007	0.105	0.074			0.064
U	0.008				0.041	0.006
Sc					0.015	
Zr	0.984				0.958	
Hf					0.014	
Σcat	2.000	2.002	2.005	15.984	1.983	2.004

1060
1061
1062
1063
1064
1065
1066
1067
1068
1069
1070
1071

Table A3

May 2018, IGG-CNR U.O.S. of Pavia

Sample	Identifier	Zrc#	Spot Position	Zoning	$^{207}\text{Pb}/^{206}\text{Pb}$	$\sigma\%$
RG12	My10b006	1	rim	oscill	0,04950	0,00148
RG12	My10b007	2	rim	oscill	0,05477	0,00202
RG12	My10b008	2	core	oscill	0,04710	0,00141
RG12	My10b009	3	rim	oscill	0,05143	0,00177
RG12	My10b010	4	rim	oscill	0,04670	0,00398
RG12	My10b011	6	rim/core	oscill	0,07078	0,00256
RG12	My10b012	5	rim	homog	0,07040	0,00209
RG12	My10b013	8	rim	oscill	0,05475	0,00170
RG12	My10b014	8	core	homog	0,04778	0,00239
RG12	My10b015	9	rim/core	oscill	0,05439	0,00224
RG12	My10b016	11	rim	oscill	0,04944	0,00150
RG12	My10b017	12	core	oscill	0,04630	0,00578
RG12	My10b018	14	rim	oscill	0,05693	0,00167
RG12	My10b019	15	rim	oscill	0,04888	0,00202
RG12	My10b020	16	rim	oscill	0,04981	0,00206
RG12	My10b021	17	rim	oscill	0,06913	0,00240
RG12	My10b026	18	rim	oscill	0,04913	0,00448
RG12	My10b027	19	rim	oscill	0,05566	0,00225
RG12	My10b028	21	rim	oscill	0,05372	0,00161
RG12	My10b029	22	rim	oscill	0,05118	0,00181
RG12	My10b030	25	rim	oscill	0,04859	0,00152
RG12	My10b031	26	rim	oscill	0,05028	0,00170
RG12	My10b032	27	rim	oscill	0,06063	0,00213
RG12	My10b033	29	rim	oscill	0,07312	0,00210
RG12	My10b034	30	rim/core	oscill	0,05588	0,00256
RG12	My10b035	31	rim	oscill	0,05122	0,00160
RG12	My10b036	32	rim	oscill	0,05050	0,00183
RG12	My10b037	33	rim	oscill	0,04789	0,00185
RG12	My17a006	34	rim	oscill.	0,05215	0,00357
RG12	My17a007	35	rim	oscill.	0,05168	0,00254
RG12	My17a009	37	rim	oscill.	0,06402	0,00329
RG12	My17a010	38	rim	oscill.	0,05069	0,00212
RG12	My17a012	42	rim	oscill.	0,04691	0,00202
RG12	My17a013	43	rim	oscill.	0,06156	0,00275
RG12	My17a014	51	rim	oscill.	0,04615	0,00706
RG12	My17a015	50	rim	oscill.	0,07062	0,00306
RG12	My17a016	52	rim	oscill.	0,06392	0,00254
RG12	My17a017	54	rim	oscill.	0,05203	0,00204
RG12	My17a018	53a	rim	oscill.	0,05625	0,00221
RG12	My17a019	53b	rim	oscill.	0,05349	0,00409
RG14	My17c006	1	rim	oscill	0,05561	0,00304
RG14	My17c007	2	rim	oscill	0,05015	0,00180
RG14	My17c008	3	rim	oscill	0,05264	0,00201

RG14	My17c009	4	rim	oscill	0,04696	0,00239
RG14	My17c010	5	rim	oscill	0,05841	0,00213
RG14	My17c011	6	rim	broad band	0,06220	0,00989
RG14	My17c012	8	rim	oscill	0,05400	0,00312
RG14	My17c013	9	rim	oscill	0,04719	0,00252
RG14	My17c014	10	rim	oscill	0,05225	0,00250
RG14	My17c015	11	rim	oscill	0,05806	0,00213
RG14	My17c016	12	rim	oscill	0,07443	0,00553
RG14	My17c017	13	rim	oscill	0,05884	0,00350
RG14	My17c018	15	rim	oscill	0,08283	0,00638
RG14	My17c019	17	rim	oscill	0,05245	0,00275
RG14	My17c020	18	rim	oscill	0,04710	0,00473
RG14	My17c021	19	rim	oscill	0,06024	0,00391
RG14	My17c022	22	rim	oscill	0,05021	0,00232
RG14	My17c023	23	rim	oscill	0,04643	0,00295
RG14	My17c024	24	rim	oscill	0,05516	0,00529
RG14	My17c025	25	rim	oscill	0,05656	0,00192
RG14	My17c026	26	rim	oscill	0,06423	0,00301
RG14	My17c027	27	rim	oscill	0,06459	0,00329
RG14	My17c029	29	rim	oscill	0,05740	0,00687
RG14	My17c030	30	rim	oscill	0,04702	0,00302
RG14	My17c031	31	rim	oscill	0,09611	0,00435
RG14	My17c036	34	rim	broad band	0,05629	0,00274
RG14	My17c037	35	rim	oscill	0,04775	0,00232
RG14	My17c039	40	rim	oscill	0,09471	0,00239
RG14	My17c040	41	rim	oscill	0,05156	0,00211
RG14	My17c041	45	core	oscill	0,05768	0,00157
RG14	My17c042	45	rim	oscill	0,04891	0,00313
RG14	My17c043	49	rim	oscill	0,04690	0,00212
RG14	My17c045	54	rim	oscill	0,04675	0,00323
RG14	My17c047	55	rim	oscill	0,04956	0,00379
RG14	My17c048	56	rim	oscill	0,06292	0,00311
RG14	My17c049	61	rim	oscill	0,05161	0,00235
RG14	My17c050	60	core	oscill	0,05264	0,00338
RG14	My17c051	59	rim	oscill	0,04619	0,00210
RG14	My17c052	58	rim	oscill	0,05184	0,00306

1073
1074

Data for Wetherill plot ³					$^{207}\text{Pb}/^{206}\text{Pb}$	\square abs
$^{207}\text{Pb}/^{235}\text{U}$	$\square\square\%$	$^{206}\text{Pb}/^{238}\text{U}$	$\square\square\%$	Rho		
0,00761	0,00021	0,00112	0,00002	0,7	171,6	5,1
0,00848	0,00030	0,00112	0,00002	0,6	402,8	14,9
0,00737	0,00020	0,00114	0,00002	0,7	54,3	1,6
0,00675	0,00022	0,00095	0,00002	0,7	260,1	8,9
0,00750	0,00063	0,00117	0,00002	0,2	33,9	2,9
0,01035	0,00035	0,00106	0,00002	0,6	951,1	34,4
0,00939	0,00026	0,00097	0,00002	0,8	940,0	27,9
0,00716	0,00021	0,00095	0,00002	0,8	402,0	12,5
0,00636	0,00031	0,00097	0,00002	0,5	88,4	4,4
0,00730	0,00029	0,00097	0,00002	0,6	387,2	16,0
0,00691	0,00020	0,00102	0,00002	0,8	168,8	5,1
0,00592	0,00073	0,00093	0,00002	0,2	13,3	1,7
0,00831	0,00022	0,00106	0,00002	0,8	488,8	14,4
0,00672	0,00026	0,00100	0,00002	0,6	142,1	5,9
0,00643	0,00025	0,00094	0,00002	0,6	186,1	7,7
0,00871	0,00028	0,00092	0,00002	0,7	902,6	31,3
0,00827	0,00075	0,00122	0,00002	0,2	154,0	14,1
0,00736	0,00028	0,00096	0,00002	0,6	438,8	17,7
0,00757	0,00021	0,00102	0,00002	0,8	359,3	10,8
0,00716	0,00025	0,00101	0,00002	0,6	248,9	8,8
0,00705	0,00021	0,00105	0,00002	0,7	128,1	4,0
0,00711	0,00023	0,00103	0,00002	0,7	208,0	7,0
0,00816	0,00027	0,00098	0,00002	0,7	626,1	22,0
0,00951	0,00026	0,00094	0,00002	0,9	1017,3	29,2
0,00837	0,00037	0,00109	0,00002	0,5	447,6	20,5
0,00756	0,00022	0,00107	0,00002	0,7	250,7	7,8
0,00699	0,00024	0,00101	0,00002	0,6	218,1	7,9
0,00666	0,00024	0,00101	0,00002	0,6	93,8	3,6
0,00732	0,00050	0,00102	0,00002	0,3	292	20,0
0,00683	0,00034	0,00096	0,00001	0,2	271	13,3
0,00854	0,00044	0,00097	0,00002	0,4	742	38,2
0,00711	0,00030	0,00102	0,00002	0,5	227	9,5
0,00620	0,00027	0,00096	0,00001	0,3	45	1,9
0,00879	0,00039	0,00104	0,00002	0,4	659	29,5
0,00693	0,00105	0,00109	0,00002	0,1	5	0,8
0,00952	0,00041	0,00098	0,00002	0,5	946	41,0
0,00821	0,00032	0,00093	0,00002	0,6	739	29,4
0,00670	0,00026	0,00093	0,00001	0,3	287	11,2
0,00736	0,00029	0,00095	0,00002	0,5	462	18,1
0,00702	0,00054	0,00095	0,00002	0,3	350	26,7
0,00844	0,00047	0,00110	0,00002	0,4	437	23,9
0,00722	0,00027	0,00104	0,00002	0,6	202	7,2
0,00762	0,00029	0,00105	0,00002	0,6	313	12,0

0,00656	0,00034	0,00101	0,00002	0,5	47	2,4
0,00790	0,00029	0,00098	0,00002	0,7	545	19,9
0,00840	0,00132	0,00098	0,00002	0,2	681	108,3
0,00726	0,00042	0,00098	0,00002	0,4	371	21,4
0,00666	0,00036	0,00102	0,00002	0,4	59	3,1
0,00707	0,00034	0,00098	0,00002	0,5	296	14,2
0,00823	0,00030	0,00103	0,00002	0,6	532	19,5
0,01110	0,00082	0,00108	0,00002	0,3	1053	78,2
0,00765	0,00046	0,00094	0,00002	0,4	561	33,4
0,01166	0,00089	0,00102	0,00002	0,3	1265	97,5
0,00688	0,00037	0,00095	0,00002	0,5	305	16,0
0,00610	0,00061	0,00094	0,00002	0,2	54	5,5
0,00776	0,00050	0,00093	0,00002	0,4	612	39,7
0,00659	0,00031	0,00095	0,00002	0,5	205	9,4
0,00651	0,00042	0,00102	0,00002	0,4	20	1,3
0,00741	0,00070	0,00098	0,00002	0,3	419	40,2
0,00745	0,00026	0,00096	0,00002	0,5	474	16,1
0,00878	0,00041	0,00099	0,00002	0,5	749	35,1
0,00901	0,00046	0,00101	0,00002	0,5	761	38,7
0,00766	0,00091	0,00097	0,00002	0,2	507	60,7
0,00720	0,00047	0,00111	0,00002	0,3	50	3,2
0,01372	0,00062	0,00104	0,00002	0,5	1550	70,1
0,00815	0,00040	0,00105	0,00002	0,5	464	22,6
0,00690	0,00034	0,00105	0,00002	0,5	87	4,2
0,01381	0,00037	0,00106	0,00002	0,8	1522	38,4
0,00690	0,00029	0,00097	0,00002	0,6	266	10,9
0,00751	0,00022	0,00094	0,00002	0,6	518	14,1
0,00659	0,00043	0,00098	0,00002	0,4	144	9,2
0,00646	0,00030	0,00100	0,00002	0,5	44	2,0
0,00620	0,00043	0,00096	0,00002	0,4	36	2,5
0,00644	0,00049	0,00094	0,00002	0,3	174	13,3
0,00755	0,00037	0,00087	0,00002	0,5	706	34,8
0,00720	0,00033	0,00101	0,00002	0,5	268	12,2
0,00728	0,00047	0,00100	0,00002	0,4	313	20,1
0,00705	0,00032	0,00111	0,00002	0,5	8	0,3
0,00704	0,00042	0,00099	0,00002	0,4	278	16,4

Ages ³				% U-Pb disc ⁴	Concordant age	□ abs
²⁰⁷ Pb/ ²³⁵ U	□ abs	²⁰⁶ Pb/ ²³⁸ U	□ abs			
7,7	0,2	7,2	0,1	6,3		
8,6	0,3	7,2	0,1	15,8		
7,5	0,2	7,3	0,1	1,5	7,3	0,30
6,8	0,2	6,1	0,1	10,4		
7,6	0,6	7,5	0,1	0,6	7,5	0,30
10,5	0,4	6,8	0,1	34,7		
9,5	0,3	6,2	0,1	34,1		
7,2	0,2	6,1	0,1	15,5		
6,4	0,3	6,2	0,1	2,9		
7,4	0,3	6,2	0,1	15,4		
7,0	0,2	6,6	0,1	6,0		
6,0	0,7	6,0	0,1	0,0	6,0	0,30
8,4	0,2	6,8	0,1	18,7		
6,8	0,3	6,4	0,1	5,3		
6,5	0,3	6,1	0,1	6,9		
8,8	0,3	5,9	0,1	32,7		
8,4	0,8	7,9	0,2	6,0		
7,4	0,3	6,2	0,1	16,9		
7,7	0,2	6,6	0,1	14,2		
7,2	0,2	6,5	0,1	10,2		
7,1	0,2	6,8	0,1	5,2		
7,2	0,2	6,6	0,1	7,7		
8,3	0,3	6,3	0,1	23,5		
9,6	0,3	6,1	0,1	37,0		
8,5	0,4	7,0	0,1	17,0		
7,6	0,2	6,9	0,1	9,9		
7,1	0,2	6,5	0,1	8,0		
6,7	0,2	6,5	0,1	3,4		
7,4	0,5	6,6	0,1	11,3		
6,9	0,3	6,2	0,1	10,5		
8,6	0,4	6,2	0,1	27,6		
7,2	0,3	6,6	0,1	8,6		
6,3	0,3	6,2	0,1	1,4	6,2	0,14
8,9	0,4	6,7	0,1	24,6		
7,0	1,1	7,0	0,1	-0,1		
9,6	0,4	6,3	0,1	34,4		
8,3	0,3	6,0	0,1	27,8		
6,8	0,3	6,0	0,1	11,6		
7,4	0,3	6,1	0,1	17,8		
7,1	0,5	6,1	0,1	13,8		
8,5	0,5	7,1	0,2	17,0		
7,3	0,3	6,7	0,2	8,3		
7,7	0,3	6,8	0,2	12,2		

6,6	0,3	6,5	0,2	2,0	6,51	0,31
8,0	0,3	6,3	0,2	21,0		
8,5	1,3	6,3	0,2	25,7		
7,3	0,4	6,3	0,2	14,0		
6,7	0,4	6,6	0,2	2,5		
7,2	0,3	6,3	0,2	11,7		
8,3	0,3	6,6	0,2	20,3		
11,2	0,8	7,0	0,2	37,9		
7,7	0,5	6,1	0,2	21,7		
11,8	0,9	6,6	0,2	44,2		
7,0	0,4	6,1	0,2	12,1		
6,2	0,6	6,1	0,2	1,9	6,06	0,30
7,8	0,5	6,0	0,1	23,7		
6,7	0,3	6,1	0,2	8,2		
6,6	0,4	6,6	0,2	0,3	6,57	0,30
7,5	0,7	6,3	0,2	15,8		
7,5	0,3	6,2	0,1	17,9		
8,9	0,4	6,4	0,2	28,1		
9,1	0,5	6,5	0,2	28,5		
7,7	0,9	6,2	0,2	19,3		
7,3	0,5	7,2	0,2	1,8	7,15	0,32
13,8	0,6	6,7	0,2	51,6		
8,2	0,4	6,8	0,2	17,9		
7,0	0,3	6,8	0,2	3,1		
13,9	0,4	6,8	0,2	51,0		
7,0	0,3	6,2	0,2	10,5		
7,6	0,2	6,1	0,1	20,3		
6,7	0,4	6,3	0,2	5,3		
6,5	0,3	6,4	0,2	1,5	6,44	0,31
6,3	0,4	6,2	0,2	1,4	6,19	0,30
6,5	0,5	6,1	0,2	7,1		
7,6	0,4	5,6	0,1	26,6		
7,3	0,3	6,5	0,2	10,7		
7,4	0,5	6,4	0,2	12,5		
7,1	0,3	7,2	0,2	-0,3	7,15	0,32
7,1	0,4	6,4	0,2	10,5		

1078
1079
1080
1081
1082 Table A4

Capsule name	4He sample (torr)	re-extract (torr)	Total 4He (cc)	Corrected	1 sigma 232Th (ng)
pan4 RG12a-01	2,0E-10	6,9E-11	4,4E-11	3,3E-11	6,1E-12
pan4 RG12a-04	2,4E-10	7,0E-11	5,7E-11	4,4E-11	6,1E-12
pan5 RG12a-07	2,2E-10	6,6E-11	5,6E-11	4,3E-11	3,3E-12
pan5 RG12a-08	1,2E-10	4,0E-11	2,0E-11	1,5E-11	3,2E-12
pan4 RG14a-01	4,4E-10	6,8E-11	1,3E-10	1,1E-10	6,3E-12
pan4 RG14a-03	1,6E-10	6,8E-11	2,9E-11	2,0E-11	6,0E-12
pan4 RG14a-05	2,4E-10	6,1E-11	5,5E-11	4,4E-11	6,1E-12
pan5 RG14a-06	1,9E-10	6,8E-11	4,7E-11	3,4E-11	3,2E-12
pan5 RG14a-07	4,9E-10	6,8E-11	1,6E-10	1,4E-10	4,1E-12
pan5 RG14a-08	2,5E-10	6,8E-11	6,9E-11	5,4E-11	3,4E-12

1083

1 sigma error 238U (ng) 1 sigma error 232Th Blk correction 1 sigma error 238U Blk correction

0,003	0,05	0,001	0,26	0,004	0,0515
0,001	0,04	0,001	0,03	0,002	0,0397
0,001	0,05	0,001	0,05	0,006	0,0484
0,001	0,04	0,001	0,05	0,006	0,0396
0,004	0,14	0,002	0,37	0,005	0,1349
0,001	0,05	0,001	0,06	0,002	0,0433
0,002	0,08	0,001	0,16	0,003	0,0728
0,000	0,08	0,002	0,03	0,006	0,0816
0,002	0,11	0,001	0,15	0,007	0,1068
0,001	0,12	0,002	0,06	0,006	0,1188

1084

1 sigma error 232Th(ppm) 238U(ppm) eU(ppm) Total analytical error (%) Reheat to heat ratio Age (Ma)

0,0009	214,774	42,332	92,804	1,19%	34,21%	3,2
0,0015	27,566	31,867	38,345	3,53%	29,09%	9,9
0,0008	62,567	58,259	72,962	6,46%	30,07%	7,6
0,0007	74,429	63,496	80,987	7,52%	33,13%	3,3
0,0017	215,778	79,401	130,109	0,97%	15,58%	4,1
0,0010	70,154	48,055	64,542	2,29%	42,77%	4,0
0,0011	110,015	50,071	75,925	1,29%	25,56%	4,1
0,0016	25,213	60,131	66,056	5,72%	35,44%	4,3
0,0012	110,644	78,040	104,041	2,61%	13,95%	9,0
0,0019	36,723	78,141	86,771	3,84%	26,72%	4,3

1085

Real age Error Th/U Error length width1 width2 width3 average width Radius Termination

2,40	0,04	5,1	0,11	160	60	50	55,0	27,5	1	
7,63	0,35	0,9	0,06	150	60	55	57,5	28,8	1	
5,81	0,49	1,1	0,13	120	55	50	52,5	26,3	0	
2,47	0,25	1,2	0,16	110	50	45	47,5	23,8	1	
3,54	0,05	2,7	0,05	160	70	65	60	65,0	32,5	2
2,84	0,09	1,5	0,06	130	55	50	52,5	26,3	1	
3,24	0,05	2,2	0,05	170	65	60	50	58,3	29,2	2
3,15	0,24	0,4	0,08	150	70	50	60,0	30,0	2	
7,93	0,24	1,4	0,06	180	60	50	55,0	27,5	2	
3,40	0,17	0,5	0,05	200	60	50	55,0	27,5	2	

1086

F(T) large (U-Th weighted)	Corrected Age	error	²³⁸ U/atoms	²³⁵ U/atoms	²³² Th/atoms	⁴ He/atoms
0,57	4,2	0,4	1,30E+11	9,57E+08	6,78E+11	1,19E+09
0,59	13,0	0,7	1,01E+11	7,38E+08	8,92E+10	1,54E+09
0,54	10,8	0,9	1,23E+11	9,00E+08	1,35E+11	1,50E+09
0,53	4,7	0,5	1,00E+11	7,36E+08	1,21E+11	5,43E+08
0,63	5,6	0,3	3,41E+11	2,51E+09	9,52E+11	3,41E+09
0,64	4,4	0,2	1,09E+11	8,04E+08	1,64E+11	7,70E+08
0,60	5,4	0,3	1,84E+11	1,35E+09	4,15E+11	1,47E+09
0,60	5,2	0,4	2,06E+11	1,52E+09	8,88E+10	1,25E+09
0,58	13,6	0,7	2,70E+11	1,98E+09	3,93E+11	4,21E+09
0,59	5,8	0,3	3,01E+11	2,21E+09	1,45E+11	1,86E+09

Average age	5,0	0,6	12%
--------------------	------------	------------	------------

1087